# Flow and fracture of austenitic stainless steels at cryogenic temperatures

P. Fernández-Pisón[a,c,*], J. A. Rodríguez-Martínez[a], E. García-Tabarés[b,c], I. Avilés-Santillana[c], S. Sgobba[c]

[a] *Department of Continuum Mechanics and Structural Analysis. University Carlos III of Madrid, Leganés, Madrid, Spain*
[b] *Department of Physics. University Carlos III of Madrid, Leganés, Madrid, Spain*
[c] *European Organization for Nuclear Research (CERN), Genève, Switzerland*

**Abstract**

In this paper, we have characterized the microstructural evolution and the plastic flow and fracture behaviours of AISI 304L and AISI 316LN stainless steel grades at liquid nitrogen temperature (77 K) and at liquid helium temperature (4 K). Uninterrupted tensile experiments, where the sample is continuously deformed under quasi-static loading conditions until fracture, have been carried out with a Single-Section Sample to obtain the stress-strain characteristics of the two grades. Interrupted tensile experiments, in which the sample is unloaded before fracture, have been performed with a novel Double-Section Sample to later characterize the strain-induced martensitic transformation at different levels of deformation. The content of martensite has been determined post-mortem, using magnetic induction, electron backscatter diffraction and quantitative light optical micrography. The results obtained with the three methods show quantitative agreement, and reveal that the martensitic transformation in AISI 304L occurs faster and to a greater extent than in AISI 316LN both at 77 K and at 4 K. To the authors' knowledge, in this paper we provide the first experimental results for the evolution of the content of strain-induced martensite in AISI 304L and AISI 316LN samples tested at liquid helium temperature. In addition, the experimental data for the evolution of the martensite volume fraction with the strain have been used to identify the temperature-dependent parameters of the martensitic transformation kinetic models proposed by Olson and Cohen (1975) and Garion and Skoczeń (2002). Moreover, Mode I fracture tests with fatigue-precracked Compact Samples have been carried out to determine the fracture properties of the two investigated materials using the "resistance curve procedure" (ASTM-E1820-20a, 2020). The crack-growth resistance curves have been obtained with four different methods here referred to as ASTM Compliance Method, W-N Compliance Method, Modified W-N Compliance Method and ASTM Normalization Method, which is an original methodological contribution of this paper. While the four approaches yield similar results for the fracture toughness, only the W-N Compliance Method and the Modified W-N Compliance Method, the latter being proposed in this paper, fulfil all the requirements of the standard ASTM-E1820-20a (2020) so that the calculated fracture toughness can be accepted as a material property. The comparison of results for both materials and testing temperatures shows that the AISI 316LN displays higher fracture toughness than the AISI 304L. Moreover, post-mortem microstructural analysis of the Compact Samples near the fracture surface has revealed that the content of martensite is greater in AISI 304L than in AISI 316LN. Furthermore, for AISI 304L more martensite is formed in the sample tested at 77 K because the plastic deformation near the crack is greater than at 4 K.

*Corresponding author. Tel. +34 916246015; Fax: +33 916249430. E-mail address:mariapilar.fernandez@uc3m.es

*Keywords:*
Austenitic stainless steels, Mechanical characterization, Fracture toughness, Strain-induced martensite, Cryogenic temperatures

## 1. Introduction

Superconducting high-field magnets have become indispensable in high-energy particle physics accelerators to accurately guide the particle beams, such as at the LHC at CERN (Brüning et al., 2012), and in fusion reactors to confine and control the plasma, such as ITER (Mitchell et al., 2008).

The magnet systems, as they are used in CERN's LHC or ITER, contain coils made of niobium-titanium (NbTi) or niobium-tin ($Nb_3Sn$) conductors, that need to be cooled to cryogenic temperatures to achieve the superconducting state (Brüning et al., 2012; Apollinari et al., 2015; Mitchell et al., 2008). Superconducting cables allow to apply very high currents that induce strong magnetic fields causing high magnetic forces within the magnet system. These forces have to be counteracted by structural components at the named cryogenic temperatures. Such components are, for instance, the steel collars of the standard Dipole magnet for the LHC (Bertinelli et al., 2006) and the jacket of the so-called ITER "Cable-In-Conduit Conductors" (Devred et al., 2014). Since austenitic stainless steels display stable material properties over the whole temperature operating range of the superconducting magnets, they are the dominant structural materials used for these components (Sgobba, 2006; Barabash et al., 2007).

Austenitic stainless steels generally retain high strength, ductility and toughness at low temperatures, and they are paramagnetic or antiferromagnetic under the Néel temperature in the fully austenitic state. Nevertheless, they are susceptible to develop strain-induced martensitic transformation, especially at cryogenic temperatures. The initially undeformed $\gamma$-austenitic phase (face-centred cubic) may be transformed, by different transformation mechanisms, either to $\alpha'$-martensite (body-centred tetragonal) or to $\epsilon$-martensite (hexagonal close packed). After a relatively low deformation, the strain-induced $\alpha'$-martensitic transformation is more extensive than the transformation of $\epsilon$-martensite (De et al., 2004; Mangonon and Thomas, 1970). Moreover, the $\alpha'$-martensitic phase is ferromagnetic and becomes brittle at cryogenic temperatures. For these reasons, the $\gamma$-$\alpha'$ transformation is a major concern due to the high impact on the performance of the structural components used in high-field magnet systems. A comprehensive analysis of the flow and fracture behaviours of austenitic stainless steels at low temperatures, as applied for the superconducting magnets used at CERN and ITER, is therefore essential.

The manuscript is organized as follows. The austenitic stainless steels AISI 304L and AISI 316LN investigated in this work are presented in Section 2, including their chemical composition and the analysis of their microstructure in the as-received condition. In Section 3, we characterize the plastic flow behaviour and microstructural evolution of AISI 304L and AISI 316LN during uniaxial tensile tests performed at 300 K, 77 K and 4 K. A detailed description of the

employed experimental techniques is provided in Section 3.1.1, and the analysis of results is performed in Section 3.1.2. The fracture behaviour of AISI 304L and AISI 316LN is investigated in Section 4. Specifically, Section 4.1 describes the Compact Sample used in the experiments, the four methods employed to construct the $J-R$ crack-growth resistance curves and the optical microscopy technique used to determine the strain-induced martensite formed near the fracture surface during the tests, while the results are presented and discussed in Section 4.2. A summary of the research including the main findings derived from this investigation is given in Section 5.

## 2. Materials

The materials studied are AISI 304L and AISI 316LN austenitic stainless steels. The AISI 304L is a general-purpose grade, while the AISI 316LN is selected for applications requiring high strength, or where an increase of magnetic susceptibility might be of concern (Vogt et al., 1991). The AISI 304L is the low (L) carbon version of the common iron-chromium-nickel AISI 304. On the other hand, the AISI 316LN is a modification of the molybdenum-containing grade AISI 316, with low (L) content of carbon and addition of nitrogen (N) (Reed, 1989). The effect of molybdenum is the improvement of corrosion resistance and a higher stability of the austenite against martensitic transformation. Nitrogen also increases austenite stability, and enhances the formation of austenite compared to ferrite. Moreover, nitrogen substantially increases strength and maintains ductility down to cryogenic temperatures (Sgobba, 2006). The specific chemical compositions of the AISI 304L and AISI 316LN grades investigated in this work are given in Table 1.

The raw materials were provided in the form of hot rolled and solution annealed plates of 12 mm thickness (surface quality according to the standard EN-10088-2 (2008) as stated in CERN Technical Specifications No. 1004-ED.6 and No. 1002-ED.5 for AISI 304L and AISI 316LN respectively). Fig. 1 shows the undeformed microstructure of both materials. Rolling direction is horizontal in the micrographs. The AISI 304L presents some linear ferrite precipitations embedded in the austenitic matrix along the rolling direction. The ferritic phase has been identified with the selective Murakami's etchant as indicated in the standard ASTM-E407-07 (2015). Indeed, according to Sgobba (2006), the AISI 304L grade normally retains some ferrite when cooled from solution annealing. Measurements with the Feritscope confirm that the ferrite volume is lower than 0.5% (see the item **Magnetic induction** in Section 3.1.2). On the other hand, the AISI 316LN is constituted of 100% austenite, which is expected due to the strong austenite stability provided by the alloying elements. The average grain size in the undeformed state is $D = 89.9$ $\mu$m for the AISI 304L and $D = 53.4$ $\mu$m for the AISI 316LN. These values were provided by the corresponding materials' certificates, which determined the average grain size according to the standard ASTM-E112-13 (2013).

The martensite start temperature ($M_s$), below which martensite starts to form spontaneously, has been estimated for both materials using the Self-Olson equation (see equation (1), alloying elements in weight-%) (Self et al., 1987). The equation yields $M_s \approx 80$ K for AISI 304L and $M_s < 0$ K for AISI 316LN, which suggests a higher austenite

| Grade | C | S | N | Cr | Ni | Mn | Si | Mo | P | Co |
|---|---|---|---|---|---|---|---|---|---|---|
| 304L | 0.013 | 0.0003 | – | 18.19 | 10.28 | 1.27 | 0.45 | – | 0.024 | 0.024 |
| 316LN | 0.009 | <0.002 | 0.19 | 17.37 | 13.09 | 1.34 | 0.28 | 2.61 | 0.024 | 0.100 |

Table 1: Chemical composition of AISI 304L and AISI 316LN (product analysis except for Co 316LN which is heat analysis, weight-% Fe balance).

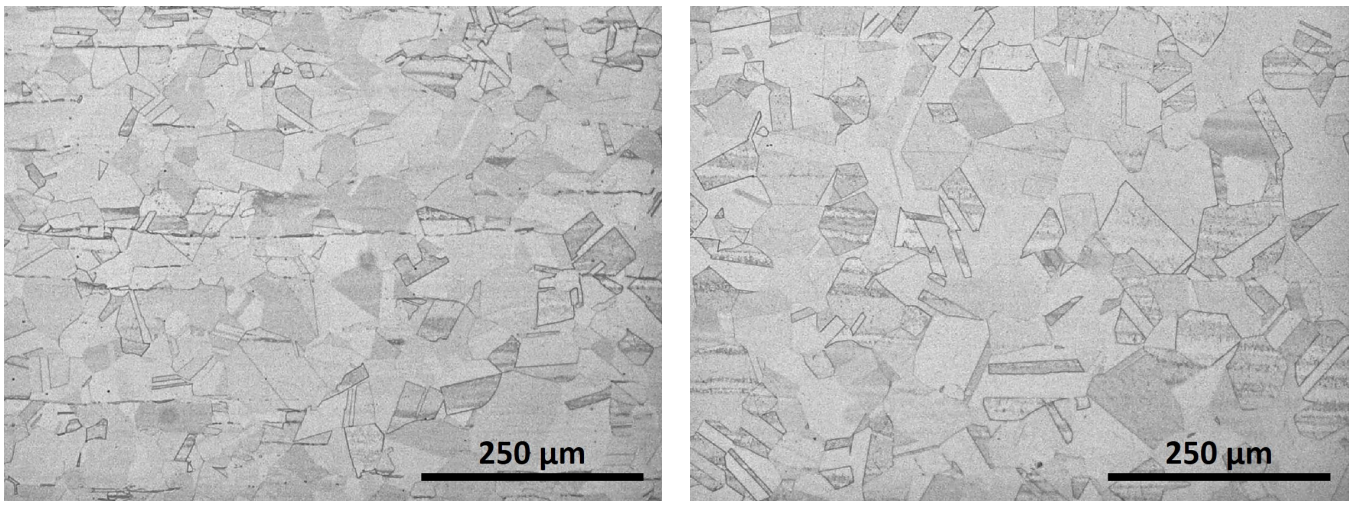


(a) (b)

Figure 1: Light optical microscopy images of the materials' cross-section (through the plate's thickness, along the rolling direction). Rolling direction is horizontal in the micrographs. Images taken after oxalic acid etching (etchant no. 13 in ASTM-E407-07 (2015)): (a) AISI 304L and (b) AISI 316LN.

stability against martensitic transformation for the AISI 316LN grade. The thermal stability of the AISI 316LN was confirmed by immersion in liquid helium for more than two hours, after which no ferromagnetic response was detected with the Feritscope thus ruling out a spontaneous martensitic transformation. Regarding the AISI 304L, there was not an evident increase of the material's ferromagnetic response neither after immersion in liquid nitrogen nor in liquid helium. Therefore, the spontaneous transformation of the AISI 304L, if any, is negligible.

$$M_s(^\circ\mathrm{C}) = 521 - 14.3\mathrm{Cr} - 17.5\mathrm{Ni} - 28.9\mathrm{Mn} - 37.6\mathrm{Si} - 350\mathrm{C} - 29.5\mathrm{Mo} + 23.1(\mathrm{Cr} + \mathrm{Mo})\mathrm{C} - 1.19\mathrm{CrNi} \quad (1)$$

## 3. Flow behaviour

In this section, we investigate the flow behaviour of both AISI 304L and AISI 316LN at 300 K, 77 K and 4 K.

### *3.1. Experimental techniques*

Different techniques have been used to characterize on the one hand the mechanical behaviour of the materials and to measure on the other hand the strain-induced $\alpha$'-martensite content. Mechanical tests consist of uniaxial tensile experiments. Martensite measuring techniques include: magnetic induction, electron backscatter diffraction (EBSD) and

quantitative light optical micrography. The martensite evaluation has been performed ex-situ at room temperature on specimens taken from the gauge length's section of deformed tensile-tested samples. All the experiments have been performed at CERN.

*3.1.1. Mechanical tests*

Uniaxial tensile tests have been performed at room temperature ($T = 300$ K), at liquid nitrogen temperature ($T = 77$ K) and at liquid helium temperature ($T = 4$ K), according to the standards ISO-6892-1 (2009), ISO-6892-3 (2015) and ISO-6892-4 (2015), respectively.

All the tests have been carried out in a 100 kN servo-hydraulic testing machine fabricated by MICROTEST, which was custom designed to integrate the pre-existing tools at CERN for cryogenic applications. Two Epsilon cryogenic extensometers (3442C-050M-020-LT) have been employed for the tests. They offer a maximum extension of 10 mm and have been used in their shortest configuration of 12.5 mm gauge length which maximises the available strain measuring range. All the tests have been performed under displacement control of the machine's cross head at constant speed, yielding for an imposed initial strain rate of approximately $\dot{\varepsilon} \approx 10^{-4}$ s$^{-1}$ (see Section 3.2). For the tests performed at room temperature, the samples have been directly attached to the machine's cross head, whereas for the cryogenic tests, the in-house developed cryostat described by Avilés-Santillana et al. (2015) and Malik (2021), has been employed. The cryostat is used as a thermal container and also as a load-bearing link that transfers the load from the cross head of the machine to the sample. It is equipped with an inlet and an outlet for the cryogenic fluid. The cryogenic fluid is continuously supplied via a cryogenic transfer line from a pressurized dewar that is equipped with a valve for flow control. The analogue signals from the internal sensors, such as the extensometers, are transmitted to the external data acquisition system (DAQ) via the cryostat's electrical connection ports. They are converted by a HBM QuantumX MX840B-DAQ and they are continuously monitored with the CATMAN software. The signal from the machine's load cell is also connected to the DAQ in order to relate the load measurement with the displacement of the extensometer. The test is started after the sample and the internal sensors are completely immersed in the cryogenic liquid medium, so that the signal of the sensors is stable due to the constant cryogenic temperature. At last, before starting the test, the cryogenic fluid flow is strongly decreased aiming to avoid perturbations in the sensors' signal caused by fluid turbulences.

The tensile samples have been extracted from the mid-thickness region of each plate with the tensile axis parallel to the rolling direction ("longitudinal flat tension test" according to the standard ASTM-A370-15 (2015)). The thickness of the samples is 4 mm. Two different geometries, here referred to as Single-Section Sample and Double-Section Sample, have been used:

- **Single-Section Sample**: it has been used in uninterrupted tensile tests where the sample is continuously deformed until fracture. The aim is to obtain the complete stress-strain curve of the material. The design of the Single-Section

Sample (Fig. 2) is based on a "non-proportional test piece" according to the standard ISO-6892-4 (2015), taking into account the selected extensometer's gauge length. For each material, two uninterrupted tensile experiments have been performed for the three different testing temperatures.

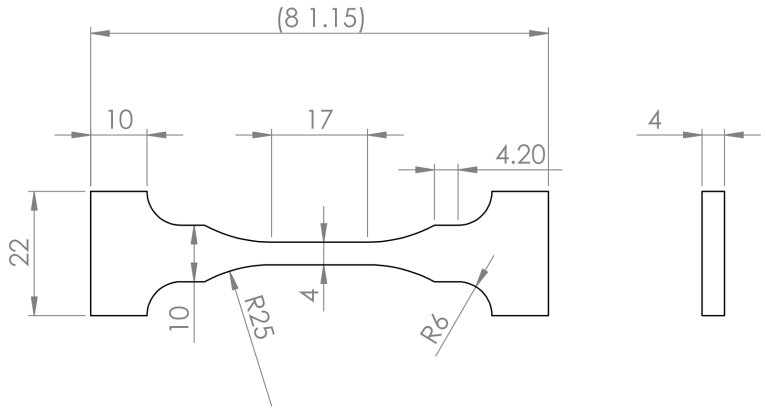


Figure 2: Design of the Single-Section Sample. Dimensions in millimetres.

- **Double-Section Sample**: it has been used in interrupted experiments in which the sample is unloaded before fracture (see Fig. 8). In a single tensile test, both gauge-length sections –which have different width– are simultaneously submitted to a different stress level. The aim is to obtain two gauge-length sections presenting different homogeneous deformation levels when the sample is unloaded, so that we later determine the strain-induced $\alpha$'-martensite (the idea is to decrease the number of experiments to be performed, since the cryogenic tests are highly time- and resources-consuming, specially helium). For reasons of comparability, both gauge sections of the Double-Section Sample have the same length, and one of them also the same width as the Single-Section Sample. The width of the other gauge section was selected based on the material's stress-strain curves previously determined by the uninterrupted tensile tests, so that we obtain eight strain levels to measure the $\alpha$'-martensite (uniformly distributed strain levels over the whole range of homogeneous strain prior the ultimate tensile strength is attained, see Fig. 6) by testing only four Double-Section Samples for each material and testing temperature. Fig. 3 shows the Double-Section Sample designed for AISI 304L and AISI 316LN. The different geometry is due to the different materials' stress-strain curve. Since the sample design is very sensitive to the material stress-strain curve, special care was taken in extracting the samples from the same position with respect to the thickness of the plate. Moreover, tight geometrical tolerances and the same machining procedure (electro-spark erosion and subsequent milling) were applied to obtain all samples. Prior to the execution of the interrupted tensile tests, a preliminary assessment of the two geometries was performed. First, tensile test simulations were performed in ABAQUS software (Dassault Systèmes Simulia Corp., RI, United States) by importing the two different geometries and the materials' stress-strain curves assessed by the uninterrupted tensile tests. Moreover, one Double-Section Sample for the AISI 304L

was tensile tested until rupture at room temperature where the full-field strain was characterized by an in-situ Digital Image Correlation analysis. Both, finite element analysis and Digital Image Correlation confirm that the strain distribution in the sample sections is largely homogeneous and that the maximum principal direction of strain is parallel to the tensile axis within each of the two different gauge-length sections (Fig. 4).

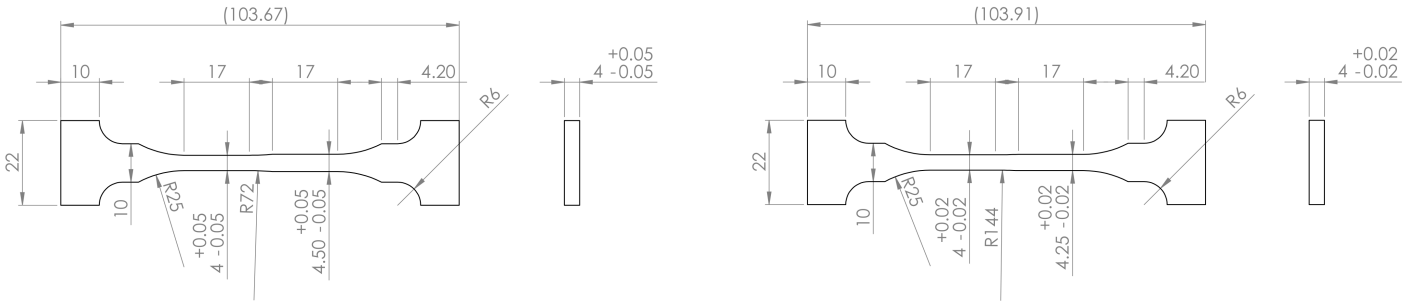


(a) (b)

Figure 3: Design of the Double-Section Sample: (a) AISI 304L and (b) AISI 316LN. Dimensions in millimetres.

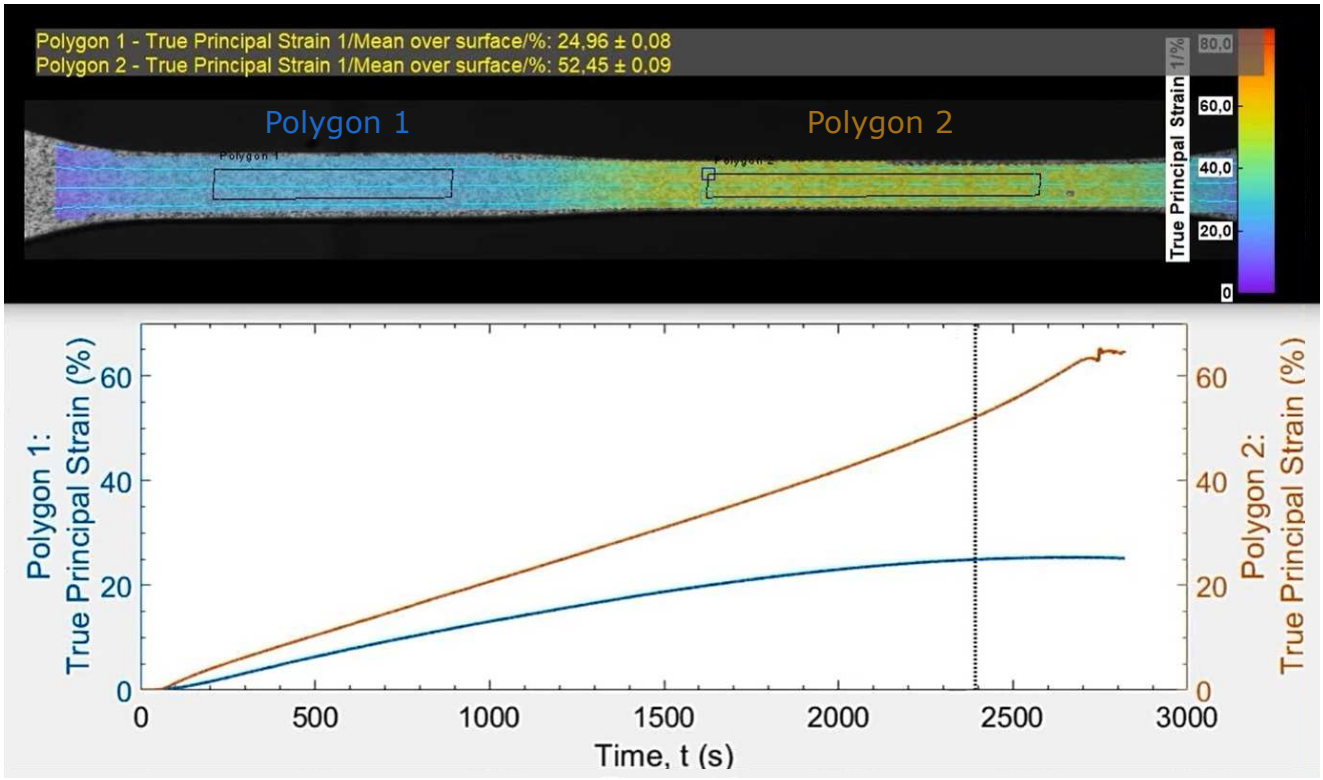


Figure 4: Strain distribution as recorded by Digital Image Correlation during tensile testing of AISI 304L Double-Section Sample (Link to the full video). The top figure shows the colour mapping of the full-field strain in the sample at a specific moment of the test (corresponding to the loading time 2400 s) including the maximum principal strain direction indicated by the cyan lines. The bottom figure shows the time evolution of the mean strain value in the respective gauge-length sections.

For all performed tensile tests, the stress has been computed using the load values from the machine's load cell (see Fig. 6). The strain values have been calculated using the displacement obtained from the extensometers: a single extensometer in the case of a Single-Section Sample, and two extensometers in the case of a Double-Section Sample.

Moreover, direct measurements of marked gauge lengths after deformation were done to verify the values computed from the extensometers.

### *3.1.2. Martensite measurements*

We have used three complementary methods to determine the martensite volume fraction in the tested specimens: magnetic induction (MI), electron backscatter diffraction (EBSD) and quantitative light optical micrography (LOM). The idea is to compare the results obtained with the three approaches, and provide consistent data for the evolution of the $\alpha$'-martensite content with the strain, for different testing temperatures.

- **Magnetic induction**

  The Feritscope locally determines the content of the ferromagnetic phase in the material using a magnetic induction probe, so that prior to the measurements the device needs to be calibrated with calibration standards of the appropriate ferromagnetic phase. In this regard, note that the Feritscope Fisher model FMP30 employed in this study was supplied with certified ferrite standards which were used for the calibration, and therefore the device provides the measurements in ferrite percent independently of the nature of the ferromagnetic phase. Moreover, according to the Feritscope manual (FERITSCOPE-FMP30, 2008), measurement readings taken at a distance less than 2 mm from the edge of the sample have to be corrected by provided correction curves. Specifically, the correction is done by multiplying the device measurements by the respective correction factor provided in the Feritscope's certificate. The Feritscope measurements have been performed in the mid-width of the section along its longitudinal direction so that, according to Ortwein (2015), when the deformed width of the sample is smaller than 4 mm, the correction has to be applied twice since the mid-width measurement is affected by the two section's edges. Taking into account that the deformed gauge-length sections present a width range between 3.25 mm and 4.42 mm for the different strain levels for which the Feritscope analysis is performed, the overall correction factor varies between 1.03 and 1.62. Note that applying the correction factor twice, as we have done in this work, or only once, leads to a change of the ferromagnetic phase quantification which is in any case smaller than 5% for all the experiments performed in this paper. Moreover, an additional correction is subsequently applied to transform the device measurements into $\alpha$'-martensite content. For that task, different calibration curves are available in the literature (Fava et al., 2018; Zheng et al., 2018; Talonen et al., 2004; Hünicke, 2000; Peterson, 1996; Hecker et al., 1982; Rintamaa, 1981). In this work, we use the bi-linear calibration curve proposed by Ortwein (2015), equation (2), where M stands for the martensite content and Fp for the ferrite percent provided by the device, both in volume-%. Note that this empirical relationship is based on the experimental data for the evolution of the $\alpha$'-martensite content with strain obtained by Talonen et al. (2004), under the assumption that the mass content of martensite is equal to its volume fraction.

$$M = \begin{cases} 1.7\,Fp & \text{if } Fp \leq 50 \\ 0.5357\,Fp + 58.2143 & \text{if } 50 \leq Fp \leq 78 \end{cases} \quad (2)$$

In order to obtain a representative value of the $\alpha$'-martensite content, eight measurements have been performed on each deformed gauge-length section of the as-tested tensile samples (four measurements per section's side). From the eight measurements, the average value has been calculated (the maximum deviation from the average is 7.4% and it corresponds to the samples tested at 4 K). Moreover, for AISI 304L the actual ferrite content present in the undeformed material has been substracted from the measurements provided by the Feritscope on the deformed material. Thus, the Feritscope readings which have been transformed to martensite contents actually correspond to the $\alpha$'-martensitic phase.

- **Electron backscatter diffraction**

Electron backscatter diffraction (EBSD) can identify and map the phases present in the microstructure based on the diffraction of electrons, generated by the scanning electron microscope (SEM), from the specific crystallographic planes. It allows the visualization of the phases' morphology and the calculation of their respective fraction on the mapped surface. However, it is a local and time-consuming technique, which needs a careful metallographic preparation of the specimen's surface to be analysed.

The specimens have been extracted from the gauge length's section of the deformed tensile-test samples. For each section, two cuts perpendicular to the sample's longitudinal direction have been performed to obtain a single 11 mm-long specimen. The cuts have been carried out by a Buehler Isomet cutting machine equipped with an alumina cutting disc using Buehler Isomet fluid as lubricant. In order to facilitate the metallographic preparation, the specimens have been mounted in a conductive resin suitable for SEM. The surface has been prepared by mechanical grinding down to 1200 grit on SiC abrasive grinding papers and mechanical polishing in three steps down to 1 $\mu$m diamond solution, followed by colloidal silica polishing. Ultrasonic cleaning with ethanol has been applied in between each step and also after the silica polishing. For reasons of comparability with the Feritscope measurements the prepared surface corresponds to one of the longitudinal-width planes of the gauge-length section. Indeed, Feritscope measurements were repeated on the prepared surfaces in order to verify that no additional martensite was formed during the preparation process. In the present study, the EBSD analyses have been performed using a ZEISS Sigma Field Emission Gun Scanning Electron Microscope (FEG-SEM) with a detector of backscattered electrons (BSE). The acquired data have been evaluated with the Oxford Instruments AZTEC-EBSD software. The SEM has been operated at 20 kV using an aperture size of 240 $\mu$m and 16.5 mm of working distance with the specimen tilted by 70°. Each map corresponds to an area of approximately 455 x 320 $\mu m^2$ which has been acquired at a magnification of 250 and has been analysed using a step size of 0.75 $\mu$m. One analysis took approximately 10 hours with the

before mentioned settings. The analyses reached a pixel indexing between 83.5% and 99.8%. The lowest indexing values correspond to specimens extracted from high deformed gauge-length sections. This can be explained by the high density of lattice defects and intrinsic dislocations that make the identification of the diffraction patterns more difficult (Ortwein, 2015; Naraghi, 2009). Note that two databases have been used for the analysis: iron body-centred cubic (Fe BCC) for martensite, and iron face-centred cubic (Fe FCC) for austenite. The reason for using BCC for identifying the martensite is due to the fact that the c/a-ratio of its actual body-centred tetragonal (BCT) lattice is very close to one (Naraghi, 2009) and the EBSD is not very sensitive to small variations of the crystallographic lattice. Thus, the content referred to as martensite in this analysis is not only accounting for the strain-induced $\alpha$'-martensite content, but as well as the ferrite that was already present in the undeformed AISI 304L material.

Only a selected number of specimens have been prepared and analysed by EBSD due to the long time needed for the specimen preparation and the analysis. The selected batch consists on 14 specimens which include for each material two deformation levels per tested temperature and a reference specimen in the undeformed state. Moreover, one single analysis has been performed for each specimen, and therefore, each result is based on a sample area of approximately 0.15 $mm^2$. The volume fraction of martensite is obtained assuming that it is equal to its area fraction.

- **Quantitative light optical micrography**

Light optical microscopy (LOM) allows to distinguish between phases with different crystallographic structure based on their different light reflection. Quantification analysis determines the fractions of the phases on the micrographs based on their different colour contrast. While this method is very sensitive to the micrograph quality, and therefore, it requires a careful and time-consuming metallographic preparation of the specimen's surface, the acquisition of the micrographs with the light optical microscope and the quantification analysis are in general fast processes. The code used for the determination of the content of martensite is included as *Supplementary Material*.

In the present study, the micrographs have been examined with a Carl ZEISS Optical Microscope connected to the ZEISS AxioCam MRc5 High Resolution Camera. Each micrograph covered an area of about 180 $\times$ 135 $\mu m^2$ which has been acquired at a magnification of 500, resulting in a pixel size of 0.13 $\mu$m. The micrographs have been taken using the specimen in the as-polished state obtained by the metallographic preparation described above, see the item **Electron backscatter diffraction**. The light optical micrographs show the martensite in dark and austenite in light (see Fig. 20 in Section 4.2). The correspondence between the two colour-contrasts and the two phases has been obtained by comparing EBSD maps with light optical micrographs covering the same sample area (the comparison is not shown here for the sake of brevity). For the phase quantification an automatic image analysis has been applied on the acquired micrographs. The image analysis method has been selected against the point count method because the latter is slower, more tedious and presents difficulties to evaluate the very fine morphology of

the strain-induced martensite (Lopez et al., 2019; Talonen et al., 2004). The automatic analysis has been applied using MATLAB software (MathWorks Inc., MA, United States). The analysis determines the martensite fraction from binary images which are obtained by image thresholding the previously processed micrographs. The final result is very sensitive to the threshold selected for the image binarization as already reported by other authors (Beese et al., 2009). In this study, the micrograph's histogram is decomposed into two Gaussian distributions, corresponding to the austenitic and martensitic phases respectively, and the threshold is defined as the white level in which both Gaussian distributions intersect (Fig. 5). Note that the histograms obtained from the micrographs show the two Gaussian distribution superposed (see Fig. 5). It means that the colour contrast of the two phases is not strongly pronounced, which is a common problem for this kind of analysis, as already reported by other authors (Talonen, 2007; Onyuna, 2003). Trials of metallographic preparations with two different products, Beraha's etchant and Ferrofluid, were performed aiming to further increase the phases' contrast on the micrographs. However, even if the contrast was increased, the results were not reproducible enough and they produced false indications. Thus, the as-polished state was selected over the etched state.

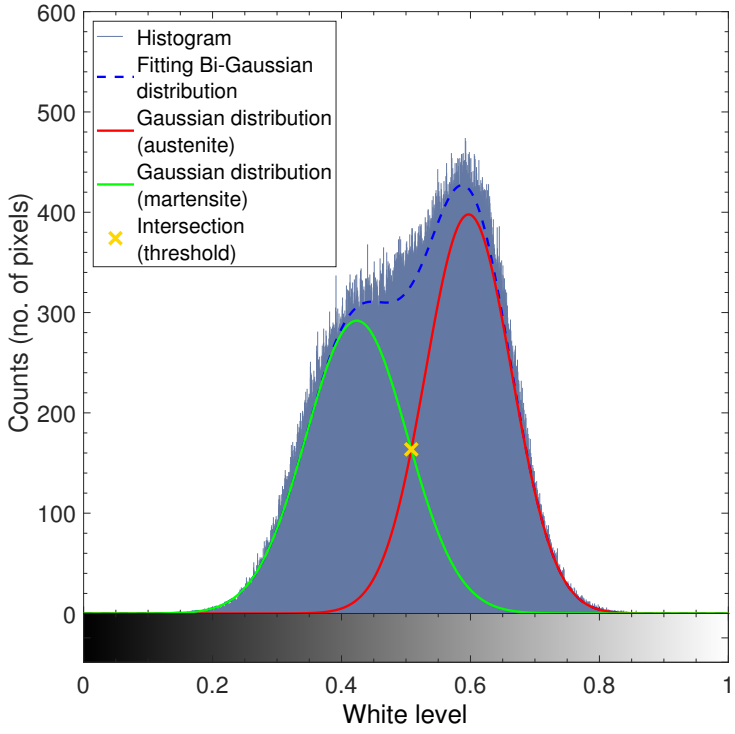


Figure 5: Histogram of a light optical micrograph showing the superposition of the two Gaussian distributions. The micrograph corresponds to the specimen AISI 304L tested at $T = 4$ K to a maximum strain level of $\varepsilon \approx 0.16$. The white level ranges from zero (black pixel) to one (white pixel).

The specimens used for the quantitative light optical microscopy analysis are the same analysed by EBSD, and therefore no additional metallographic preparation was needed. For this analysis, 24 micrographs per specimen have been acquired. For the sake of reproducibility, each of the 24 micrographs has been taken at approximately the

same surface's position on the different specimens. The quantification analyses have been performed on individual processed micrographs which cover an area of approximately 165 x 125 $\mu$m$^2$. From the 24 analyses per specimen, the martensite content for each specimen is based on an a total sample area of approximately 0.50 mm$^2$. The volume fraction of martensite is obtained assuming that it is equal to its area fraction.

### *3.2. Results*

Fig. 6 shows uniaxial tension stress-strain curves, $\sigma - \varepsilon$, obtained from AISI 304L and AISI 316LN samples tested at different temperatures $T$ = 4 K, 77 K and 300 K. The stress is the Cauchy stress computed from the machine's load cell and the strain, hereinafter also referred to as raw strain, is the Hencky strain calculated from the displacement values acquired by the extensometer, as mentioned in Section 3.1.1. The imposed initial strain rate in the experiments is $\dot{\varepsilon} \approx 10^{-4}$ s$^{-1}$ (see Section 3.1.1). The results correspond to uninterrupted tests performed with the Single-Section Sample (see Section 3.1.1). For the sake of clarity in the presentation of data, we only show one stress-strain curve per material and testing temperature. In this regard, note that the experiments showed good repeatability and the differences in the stress-strain characteristics obtained from different samples tested at the same temperature are small, and do not affect the discussion of results presented below. Notice that, for both materials, decreasing the testing temperature from 300 K to 4 K leads to a significant increase of the flow stress, favouring early necking formation and decreasing the sample ductility. The comparison of the stress-strain curves obtained in this work with data available in the literature is performed in Appendix A.

Fig. 6(a) shows the results corresponding to AISI 304L. At room temperature, the material displays an initial 0.2% offset yield strength of $\sigma_{YS} \approx 300$ MPa and quasi-linear strain-hardening, so that the necking forms at a strain of $\approx 0.51$ and the ultimate tensile strength is $\sigma_{TS} \approx 1000$ MPa (both initial yield stress and ultimate tensile strength are determined following the procedure detailed in ASTM-E8/E8M-15a (2015) converting the values to true stress, necking is assumed to start when the ultimate tensile strength is reached). At 77 K the initial 0.2% offset yield strength is $\approx 350$ MPa and the stress-strain characteristic displays a sigmoidal shape, with a sudden increase of the strain-hardening rate at a strain of $\approx 0.07$. The ultimate tensile strength is $\approx 1900$ MPa and the necking strain $\approx 0.30$. The change of curvature of the stress-strain curve and and loss of ductility are typical of a material in which the $\alpha$'-martensite fraction increases rapidly with strain (Skoczeń, 2001; Morris Jr et al., 1992), as it will be shown later (see Fig. 15). At 4 K the stress-strain curve is further shifted upwards, and the plastic flow becomes discontinuous. The phenomenon of serrated yielding –which is observed mainly in FCC metals and alloys during plastic deformation at extremely low temperatures close to absolute zero– is caused by the local formation of lattice barriers in the weakly excited lattice whose catastrophic failure leads to massive motion of the released dislocations (Tabin et al., 2016; Obst and Nyilas, 1991).

Fig. 6(b) shows the results corresponding to AISI 316LN. At room temperature, the stress-strain curve is similar to the AISI 304L, with quasi-linear strain-hardening and significant ductility, the necking strain and the ultimate tensile

strength being ≈ 0.32 and ≈ 900 MPa, respectively. At 77 K the flow stress of AISI 316LN rises significantly –the initial 0.2% offset yield strength and the ultimate tensile strength reaching ≈ 700 MPa and ≈ 2100 MPa, respectively– while keeping linear strain hardening and large ductility (unlike the AISI 304L). Decreasing the testing temperature up to 4 K further increases the material flow stress and decreases the necking strain so that the ultimate tensile strength corresponds to a strain of ≈ 0.34. Notice that the flow stress shows serrations for strains greater than 0.1. Nevertheless, for some of the experiments performed with the AISI 316LN samples at 4 K, the serrated yielding started earlier, for $\varepsilon \approx 0.05$.

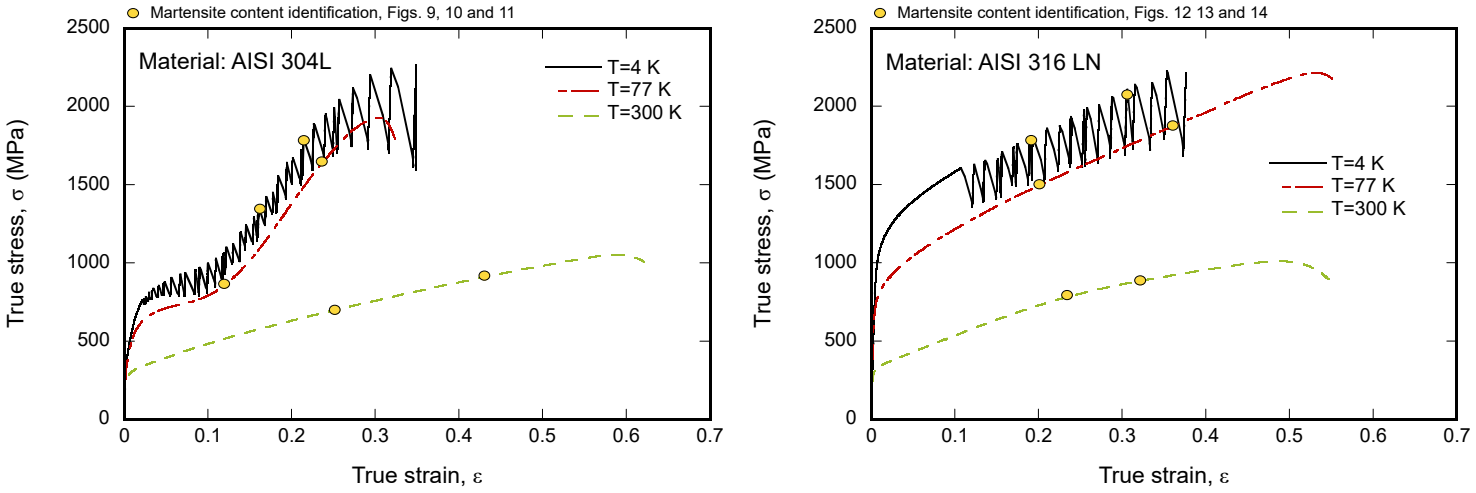


Figure 6: Stress-strain curves for three different testing temperatures $T = 4$ K, 77 K and 300 K. The imposed initial strain rate in the experiments is $\dot{\varepsilon} \approx 10^{-4}$ s$^{-1}$. Results corresponding to: (a) AISI 304L and (b) AISI 316LN. The yellow markers indicate the values of strain corresponding to the EBSD maps of Figs. 9-14.

The discontinuous plastic flow leads to simultaneous stepwise increases of strain and abrupt drops of stress with respect to time during the tests, so that the strain at 4 K is not uniform along the sample's gauge-length but rather has a local nature, as illustrated in Fig. 7, which shows the evolution of the stress (black solid line) and the raw strain (red solid line) with the loading time, for the same tests at 4 K presented in Fig. 6. As mentioned before, the raw strain is calculated from the displacement values obtained with the extensometer. The graphs also picture the evolution of the uniform strain, which is computed averaging the strain rate over time along the sample's gauge length (green dashed line), where the strain rate is calculated as the ratio between the increase of strain within a time interval. Notice that both AISI 304L and AISI 316LN samples show the same uniform strain rate $\dot{\varepsilon}$ at the beginning of loading (the initial strain rate being $\approx 10^{-4}$ s$^{-1}$ as mentioned in Section 3.1.1). However, while for the AISI 316LN samples the strain rate is *roughly* constant during the whole loading process –actually, there is a gradual decay of the strain rate due to the sample elongation–, in the case of the AISI 304L samples tested at cryogenic temperatures the uniform strain rate suddenly decreases to half of its value at $\varepsilon \approx 0.07$ (at the kink indicated in Fig. 7(a)). Notice that this is the strain value for which the stress-strain curve changes from concave-downwards to concave-upwards, see Fig. 6(a). The drop of the strain

rate occurs because the sections of the sample with $\varepsilon > 0.07$ need higher stress increment to keep deforming than the sections with a lower strain level, so that the contribution of the sections of the sample beyond the gauge length to the total sample elongation increases (see the thermodynamic considerations derived from the tensile experiments on AISI 304 samples performed by Tabin et al. (2016)). Consequently, since the velocity of the machine's cross-head is constant, the uniform strain rate on the sample's gauge length decreases.

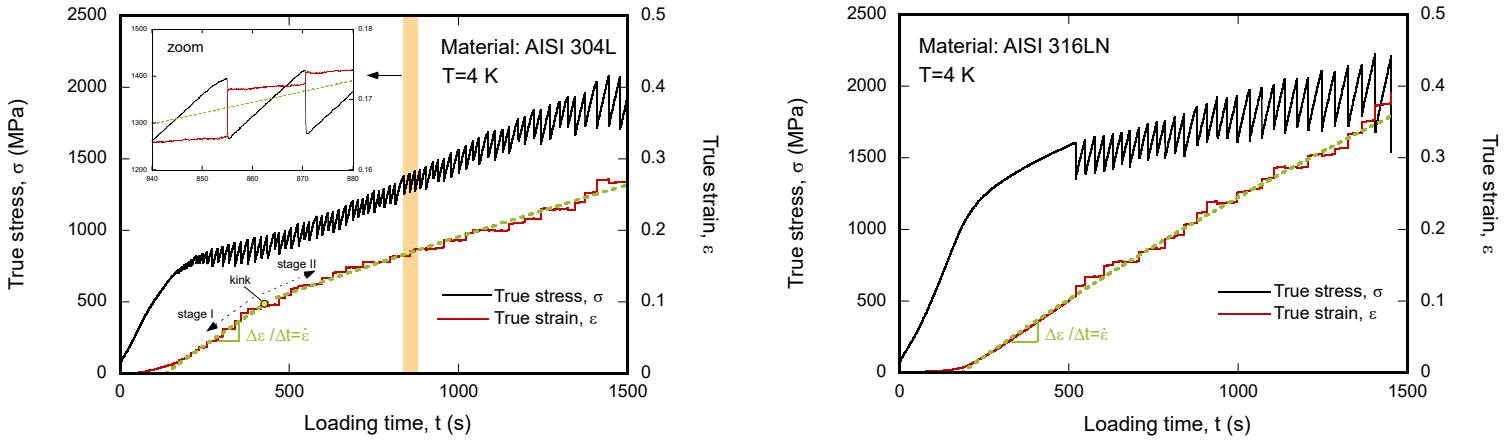


Figure 7: Temporal evolution of the stress and the strain for experiments performed at 4 K using the Single-Section Sample. The green dashed lines represent the uniform strain on the sample's gauge-length section during plastic deformation (two-stage strain rate for the case of the AISI 304L within the range of strains analysed in the figure). Results corresponding to: (a) AISI 304L and (b) AISI 316LN.

Fig. 8 shows experimental results for AISI 304L obtained at 77 K with the Double-Section Sample. Notice that the stress-strain curves computed from interrupted tests performed with the Double-Section Sample –coloured lines– and from uninterrupted tests carried out with the Single-Section Sample –black lines– are very similar. Solid coloured lines correspond to the results of the 4 mm width gauge-length section of the sample, and dashed coloured lines to the 4.5 mm width section. Each colour corresponds to the results obtained from a given Double-Section Sample. As anticipated in Section 3.1.1, performing four interrupted tests enables to obtain a set of eight distributed strain levels to measure the $\alpha$'-martensite content in the samples before the ultimate tensile strength of the material is attained: two levels of strain at the end of each test, corresponding to the two gauge-length sections of the sample. Similar observations are derived from the tests performed at 4 K and 300 K, and also from the interrupted experiments conducted with the Double-Section Sample designed for AISI 316LN.

Figs. 9-14 show EBSD maps obtained from Double-Section Samples which were used in interrupted experiments performed at different testing temperatures. The results for AISI 304L are pictured in Figs. 9-11, and the results for AISI 316LN in Figs. 12-14, respectively. For the visualization of the maps, the standard noise reduction routine for zero solution points available in the EBSD software has been applied. The colour coding of the EBSD maps is such that the

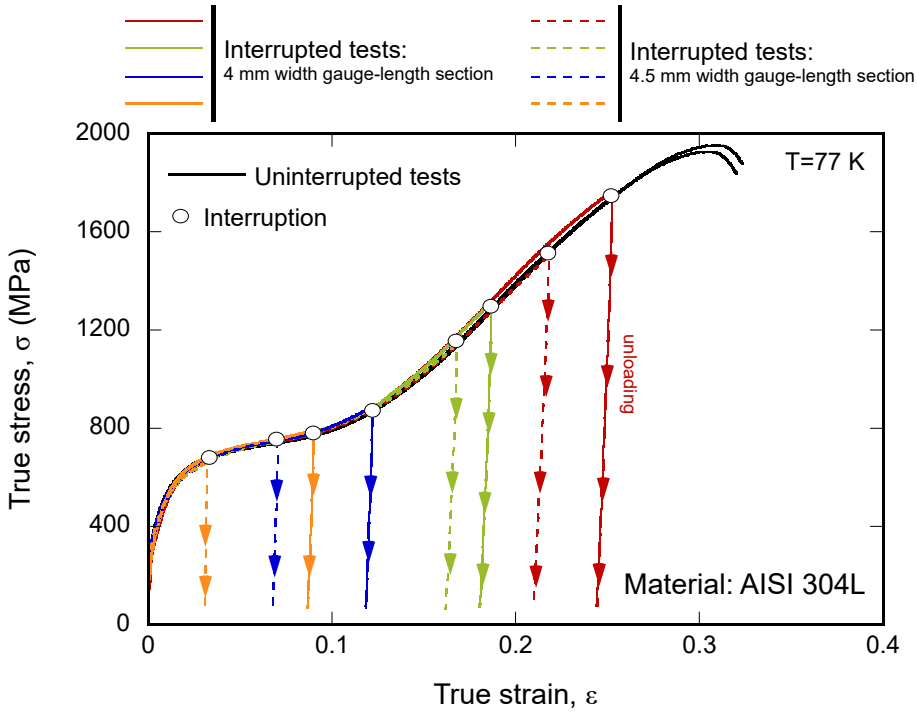


Figure 8: Experimental results for AISI 304L at 77 K. Comparison between stress-strain curves obtained from interrupted tests performed with the Double-Section Sample –coloured lines– and from uninterrupted tests carried out with the Single-Section Sample –black lines–. Solid coloured lines correspond to the results of the 4 mm width gauge-length section, and dashed coloured lines correspond to the 4.5 mm width section. Each colour corresponds to the results obtained from a given Double-Section Sample.

martensite is in blue and the austenite is in red. The observed morphology of the $\alpha$'-martensite phase consists of the low-carbon lath-type martensite. The laths tend to align parallel to one another forming a packet arrangement. Moreover, several lath-packages with different orientations normally coexist in a single austenite grain (Naraghi, 2009; Vander Voort et al., 2004). From the EBSD maps analysed here, the lath-packages are distinguishable for specimens containing relative small contents of martensite (up to approximately 30%). Specimens containing a high content of martensite (higher than 80%) show austenite grains which are quasi-fully transformed into martensite.

Figs. 9(a)-(b) show images for an AISI 304L sample tested at 300 K corresponding to two values of strain, 0.25 and 0.43, respectively. While the amount of martensite is not large, these images make apparent the increasing formation of martensite in AISI 304L due to the accumulation of plastic deformation at room temperature. On the other hand, the amount of martensite significantly increases at cryogenic temperatures. Figs. 10(a)-(b) show EBSD maps corresponding to a sample tested at 77 K, which reveal a large martensite content for a relatively low strain of $\approx 0.12$, and quasi-complete transformation of the austenite grains into martensite at a strain of $\approx 0.24$. Moreover, the results obtained from the tests performed at 4 K, see Figs. 11(a)-(b), are similar to the EBSD maps of the tests at 77 K with the material becoming almost fully martensitic for strains greater than 0.2.

Figs. 12(a)-(b) shows EBSD maps for an AISI 316LN sample tested at 300 K which reveal that, unlike in the case of AISI 304L, negligible amount of martensite is formed in this steel grade at room temperature. On the other hand, decreasing the testing temperature promotes the martensitic transformation, yet, the content of martensite in

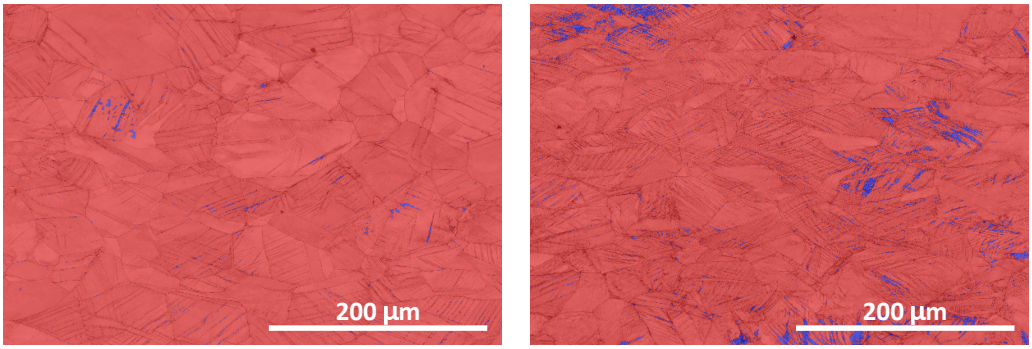


(a) (b)

Figure 9: EBSD maps of deformed AISI 304L Double-Section Sample tested at 300 K. Colour coding: martensite in blue and austenite in red. The maps correspond to different values of strain indicated in Fig. 6(a) with yellow markers: (a) $\varepsilon \approx 0.25$ and (b) $\varepsilon \approx 0.43$.

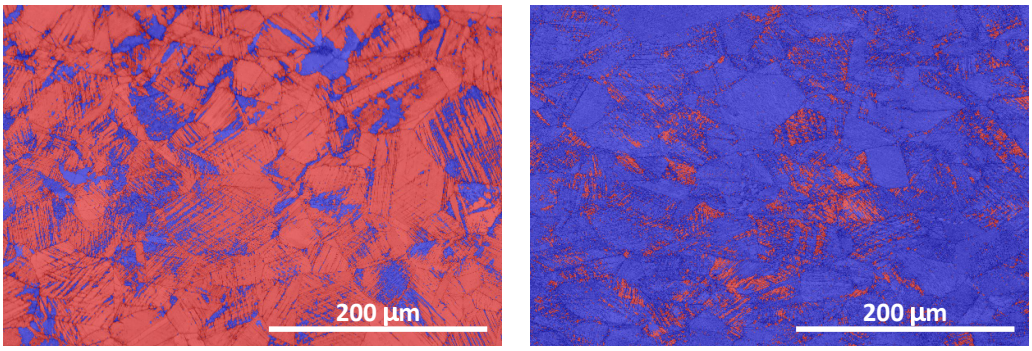


(a) (b)

Figure 10: EBSD maps of deformed AISI 304L Double-Section Sample tested at 77 K. Colour coding: martensite in blue and austenite in red. The maps correspond to different values of strain indicated in Fig. 6(a) with yellow markers: (a) $\varepsilon \approx 0.12$ and (b) $\varepsilon \approx 0.24$.

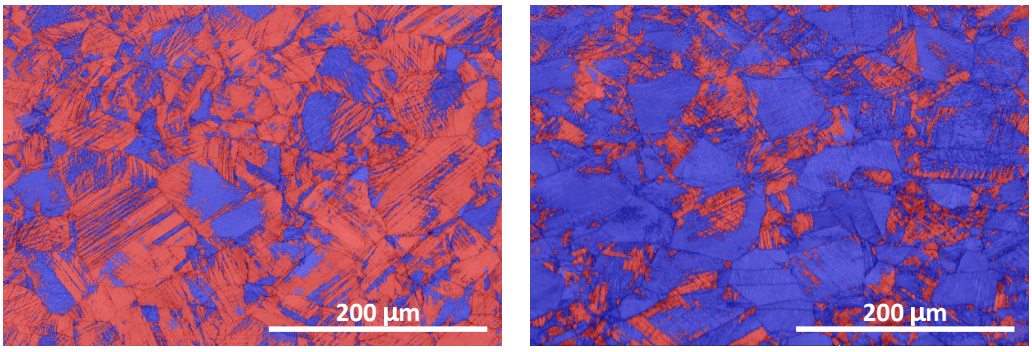


(a) (b)

Figure 11: EBSD maps of deformed AISI 304L Double-Section Sample tested at 4 K. Colour coding: martensite in blue and austenite in red. The maps correspond to different values of strain indicated in Fig. 6(a) with yellow markers: (a) $\varepsilon \approx 0.16$ and (b) $\varepsilon \approx 0.22$.

AISI 316LN samples tested at cryogenic temperatures is significantly lower than in the case of AISI 304L. Namely, the results presented in Figs. 13(a)-(b) for a test carried out at 77 K show that for a strain of $\approx 0.20$ the martensite content is virtually negligible, and that increasing the material straining up to 0.36 only causes a modest portion of the austenite to transform into martensite. Moreover, the EBSD maps of Figs. 14(a)-(b) show that the formation of martensite at 4 K starts at a lower level of strain in comparison with the test performed at 77 K (compare Figs. 13(a) and 14(a)), and the transformation seems to be faster (compare Figs. 13(b) and 14(b)).

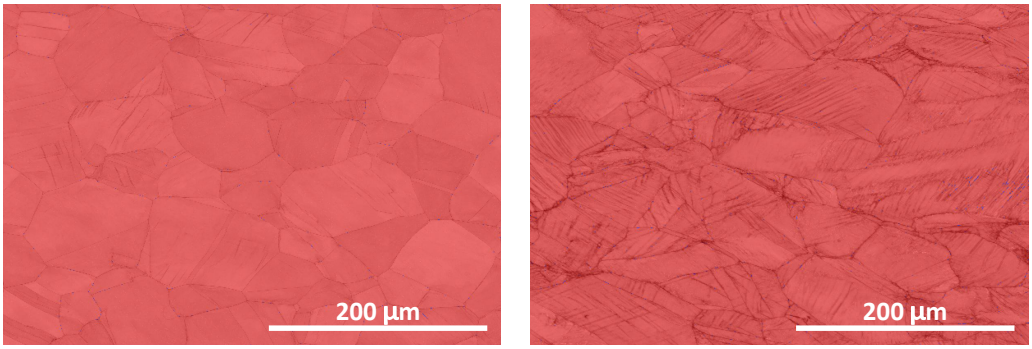


(a) (b)

Figure 12: EBSD maps of deformed AISI 316LN Double-Section Sample tested at 300 K. Colour coding: martensite in blue and austenite in red. The maps correspond to different values of strain indicated in Fig. 6(b) with yellow markers: (a) $\varepsilon \approx 0.23$ and (b) $\varepsilon \approx 0.32$.

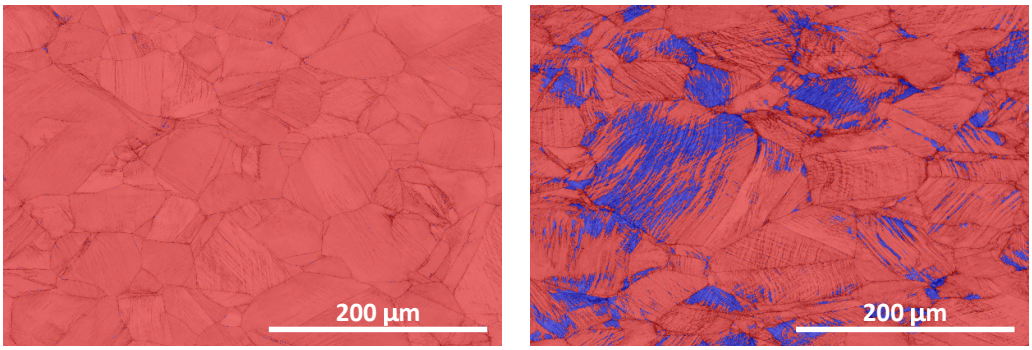


(a) (b)

Figure 13: EBSD maps of deformed AISI 316LN Double-Section Sample tested at 77 K. Colour coding: martensite in blue and austenite in red. The maps correspond to different values of strain indicated in Fig. 6(b) with yellow markers: (a) $\varepsilon \approx 0.20$ and (b) $\varepsilon \approx 0.36$.

Quantitative measurements for the evolution of the martensitic transformation with the strain (elastic strains are neglected, so that all the strain is considered to be plastic) are shown in Figs. 15 and 16. The data correspond to measurements obtained with all the three methods: magnetic induction, electron backscatter diffraction and quantitative light optical micrography (black, red and green markers, respectively). Notice that the results obtained with the three methods are similar, for the three testing temperatures (300 K, 77 K and 4 K) and both materials, which shows the robustness and reliability of the measurements. The comparison of the martensite content obtained in this work with data available in the literature is performed in Appendix A.

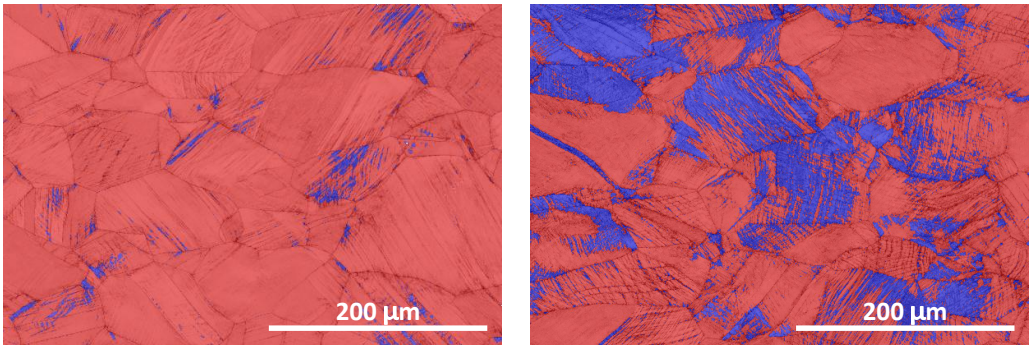


(a) (b)

Figure 14: EBSD maps of deformed AISI 316LN Double-Section Sample tested at 4 K. Colour coding: martensite in blue and austenite in red. The maps correspond to different values of strain indicated in Fig. 6(b) with yellow markers: (a) $\varepsilon \approx 0.18$ and (b) $\varepsilon \approx 0.31$.

Fig. 15 pictures the results corresponding to AISI 304L. At room temperature the martensitic transformation starts at $\varepsilon \approx 0.05$ and increases with the strain so that for $\varepsilon \approx 0.4$ the volume fraction of martensite $f^{\alpha'}$ reaches $\approx 5\%$. The evolution of the martensite content with the strain is very similar for 77 K and 4 K, with the martensite volume fraction $f^{\alpha'}$ reaching $\approx 70\%$ for a strain of $\approx 0.2$ (see Figs. 10(b) and 11(b)). The rapid martensitic transformation displayed by the AISI 304L at cryogenic temperatures explains the sigmoidal shape of the stress-strain curves shown in Fig. 6, so that the higher strength of the martensitic phase, in comparison with the austenite, is responsible for the sudden increase of the strain-hardening rate of the material. To the authors knowledge these are the first measurements available in the open literature for the martensite content in 304L tensile samples tested at 4 K.

Fig. 16 presents the results for AISI 316LN. The three measurements methods detected martensite formation at room temperature lower than 0.3% (which is within the error of the experimental measure), which evidences the higher stability of this material, in comparison with the AISI 304L, against martensitic transformation (see Fig. 12 versus Fig. 9). Moreover, unlike in the case of AISI 304L, there are significant differences in the kinetics of the martensitic transformation at 77 K and 4 K, so that the formation of martensite starts earlier and develops faster at the lower temperature. Namely, at 77 K the volume fraction of martensite for $\varepsilon = 0.2$ and 0.3 is $\approx 2\%$ and 15%, while at 4 K is $\approx 7\%$ and 25%, respectively. Nevertheless, the rate of the transformation, and the volume fraction of austenite transformed into martensite, are smaller than in the case of AISI 304L. In this regard, Morris Jr et al. (1992) and Skoczeń (2001) stated that a slow martensitic transformation does not produce a significant change on the strain-hardening rate of the material and enhances tensile ductility, in agreement with the stress-strain curves shown in Fig. 6(b) –compare the results with Fig. 6(a) for the AISI 304L–. To the authors knowledge these are the only measurements available in the literature for the martensite formation in 316LN samples tested at 4 K.

The experimental data for the evolution of the martensite volume fraction with the strain (recall that elastic strains are neglected) are fitted using the sigmoidal-type kinetic relationship proposed by Olson and Cohen (1975) and the

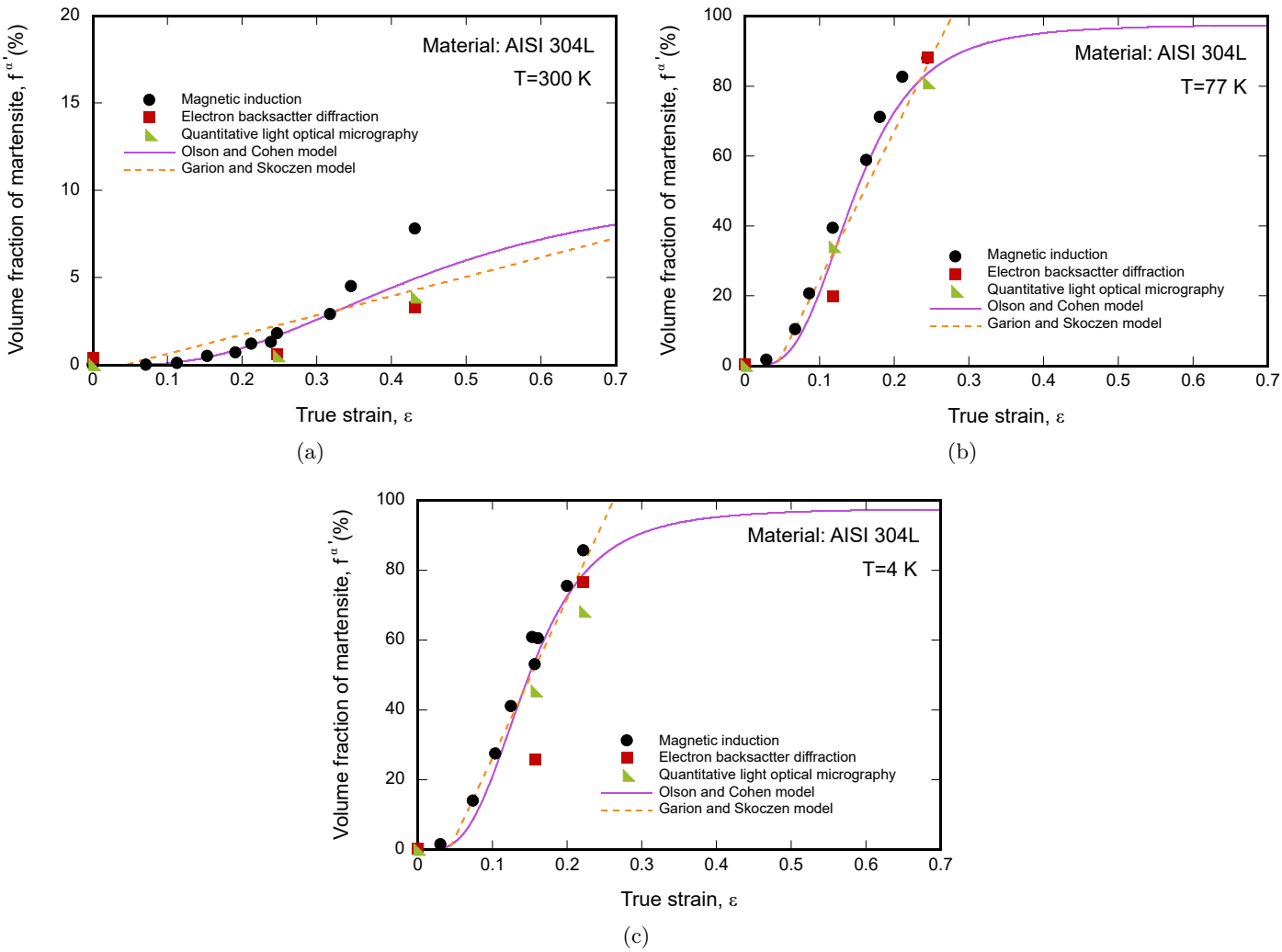


Figure 15: Evolution of the volume fraction of martensite $f^{\alpha'}$ with the strain $\varepsilon$ in AISI 304L samples tested at different temperatures: (a) 300 K, (b) 77 K and (c) 4 K. The experimental data correspond to measurements obtained with all the three methods: magnetic induction, electron backscatter diffraction and quantitative light optical micrography (black, red and green markers, respectively). Solid and dashed lines correspond to the kinetic relations of Olson and Cohen (1975) and Garion and Skoczeń (2002) which have been fitted to the experimental data (see Tables 2 and 3).

simplified linear model proposed by Garion and Skoczeń (2002), here referred to as OC and GS models, respectively, see Figs. 15 and 16. The OC model is given by equation (3), where the parameter $\alpha$ represents the rate of shear-band formation and $\beta$ indicates the probability that an intersection of shear bands will result in the nucleation of martensite. Equation (4) describes the GS model, where the parameter $A$ represents the increase of the volume fraction of martensite with respect to strain, $B$ is the critical strain which triggers the formation of martensite and $H$ denotes the Heaviside Step Function (note that we do not consider the "martensite content limit" included in equation (4) of Garion and Skoczeń (2002) since the volume fraction of martensite in the experiments shown in Figs. 15 and 16 is an increasing function of the strain).

$$f^{\alpha\prime} = 1 - e^{-\beta\left(1-e^{(-\alpha\varepsilon)}\right)^{4.5}} \tag{3}$$

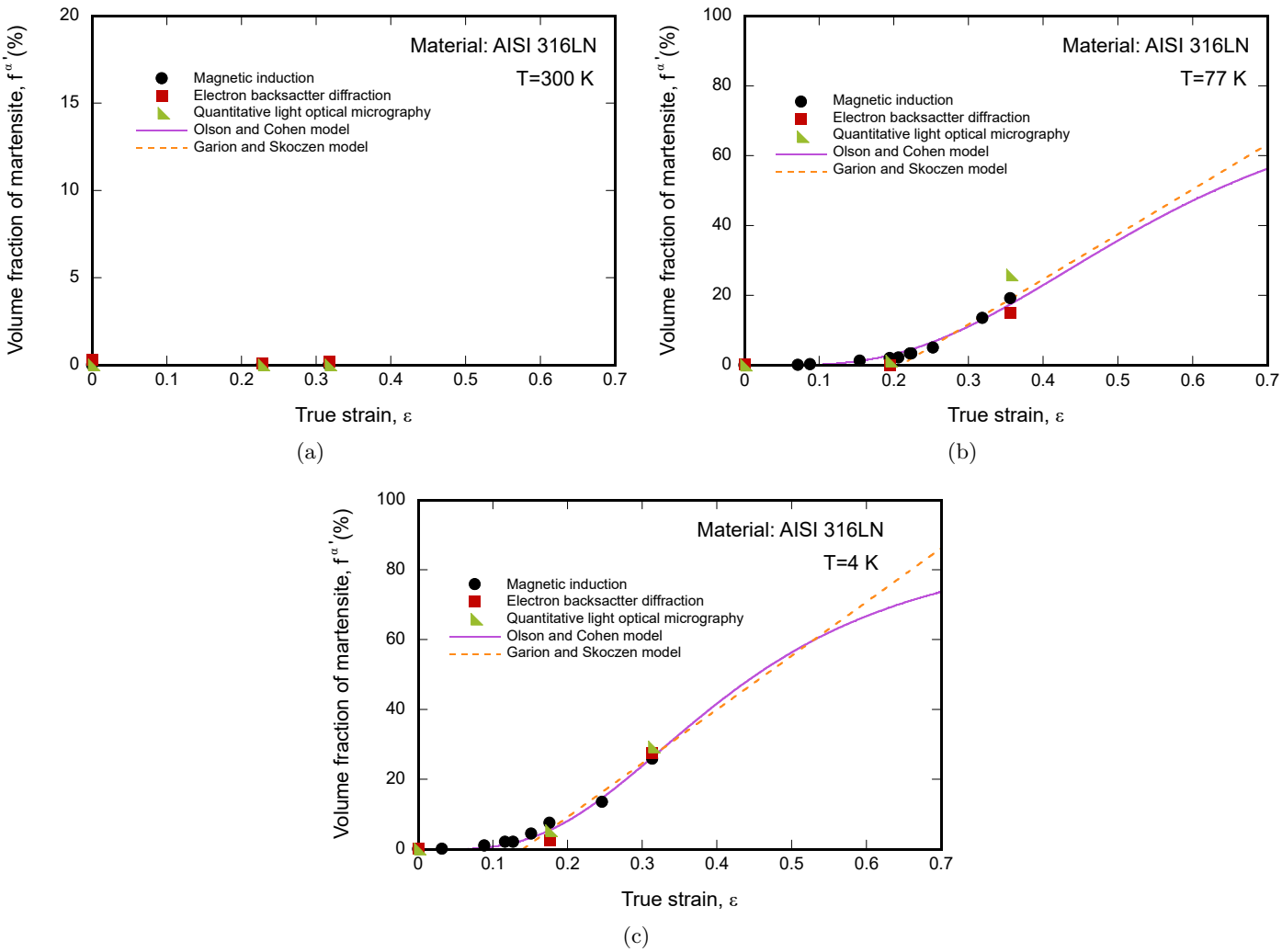


Figure 16: Evolution of the volume fraction of martensite $f^{\alpha'}$ with the strain $\varepsilon$ in AISI 316LN samples tested at different temperatures: (a) 300 K, (b) 77 K and (c) 4 K. The experimental data correspond to measurements obtained with all the three methods: magnetic induction, electron backscatter diffraction and quantitative light optical micrography (black, red and green markers, respectively). Solid and dashed lines correspond to the kinetic relations of Olson and Cohen (1975) and Garion and Skoczeń (2002) which have been fitted to the experimental data (see Tables 2 and 3).

$$f^{\alpha\prime} = A(\varepsilon - B)H\left(\varepsilon - B\right) \tag{4}$$

The values of the models' parameters are given in Tables 2 and 3. The identification process has been carried out by assuming a temperature-evolution function for each parameter. The selected functions are based on the former experimental data provided by Olson and Cohen (1975) and Garion et al. (2006). Namely, Olson and Cohen (1975) showed a dependence of the parameters $\alpha$ and $\beta$ on temperature –see Fig. 2 therein– which in this work are approximated with a half sigmoid and a full sigmoid function, respectively, see equation (5). On the other hand, while Garion et al. (2006) assumed linear interpolations between the analysed temperatures for the parameters $A$ and $B$ –see Fig. 14 therein–, in this work we use a second-degree polynomial function with respect to the temperature, see equation (6). This function improves the data fitting in comparison with a linear interpolation.

| | | AISI 304L | | | AISI 316LN | | |
|---|---|---|---|---|---|---|---|
| | | **T = 300 K** | **T = 77 K** | **T = 4 K** | **T = 300 K** | **T = 77 K** | **T = 4 K** |
| **OC** | $\boldsymbol{\alpha}$ | 4.49 | 7.81 | 7.81 | 0.37 | 2.64 | 3.38 |
| | $\boldsymbol{\beta}$ | 0.10 | 3.74 | 3.74 | 0.00 | 1.80 | 2.08 |
| **GS** | $\boldsymbol{A}$ | 0.11 | 4.26 | 4.55 | 0.00 | 1.29 | 1.54 |
| | $\boldsymbol{B}$ | 0.04 | 0.04 | 0.04 | 0.80 | 0.21 | 0.14 |

Table 2: Identification of the parameters corresponding to the kinetic relations of Olson and Cohen (1975) and Garion and Skoczeń (2002), see equations (3) and (4), used in the fitted curves shown in Fig. 15 and Fig. 16.

| | | AISI 304L | AISI 316LN |
|---|---|---|---|
| **OC** | $\boldsymbol{\alpha_1}$ | $3.36 \cdot 10^{2}$ | $3.36 \cdot 10^{2}$ |
| | $\boldsymbol{\alpha_2}$ | $1.56 \cdot 10^{1}$ | $9.32 \cdot 10^{2}$ |
| | $\boldsymbol{\alpha_3}$ | $-3.66 \cdot 10^{-2}$ | $-4.36 \cdot 10^{-5}$ |
| | $\boldsymbol{\beta_1}$ | $2.71 \cdot 10^{2}$ | $1.24 \cdot 10^{2}$ |
| | $\boldsymbol{\beta_2}$ | 3.74 | 2.10 |
| | $\boldsymbol{\beta_3}$ | $-1.25 \cdot 10^{-1}$ | $-3.73 \cdot 10^{-2}$ |
| **GS** | $\boldsymbol{A_1}$ | $-4.93 \cdot 10^{-5}$ | $-7.87 \cdot 10^{-6}$ |
| | $\boldsymbol{A_2}$ | $-2.22 \cdot 10^{-14}$ | $-1.78 \cdot 10^{2}$ |
| | $\boldsymbol{A_3}$ | 4.55 | 1.80 |
| | $\boldsymbol{B_1}$ | $2.22 \cdot 10^{-14}$ | $5.82 \cdot 10^{-6}$ |
| | $\boldsymbol{B_2}$ | $-1.92 \cdot 10^{-1}$ | $-4.03 \cdot 10^{1}$ |
| | $\boldsymbol{B_3}$ | $4.19 \cdot 10^{-2}$ | $1.28 \cdot 10^{-1}$ |

Table 3: Identification of the parameters corresponding to the kinetic relations of Olson and Cohen (1975) and Garion and Skoczeń (2002), see equations (5) and (6), used in the fitted curves shown in Fig. 15 and Fig. 16.

$$\alpha = \frac{\alpha_2}{1 + e^{[-\alpha_3(T-\alpha_1)]}} - \frac{\alpha_2}{2}; \quad \beta = \frac{\beta_2}{1 + e^{[-\beta_3(T-\beta_1)]}}; \quad \alpha_1 \geq 0; \quad \alpha_2 \geq 0; \quad \alpha_3 \leq 0; \quad \beta_2 \geq 0; \quad \beta_3 \leq 0 \tag{5}$$

$$A = A_1(T - A_2)^2 + A_3; \quad B = B_1(T - B_2)^2 + B_3; \quad A_1 \leq 0; \quad A_2 \leq 0; \quad B_1 \geq 0; \quad B_2 \leq 0; \quad B_3 \geq -B_1 B_2^2 \tag{6}$$

## 4. Fracture behaviour

In this section, we investigate the fracture behaviour of both AISI 304L and AISI 316LN steel grades at cryogenic temperatures, $T = 77$ K and $T = 4$ K.

### *4.1. Experimental techniques*

We have performed Mode I fracture tests to identify the fracture toughness of the investigated materials using four different methods, here referred to as ASTM Compliance Method, W-N Compliance Method, Modified W-N Compliance

Method and ASTM Normalization Method. Moreover, post-mortem analysis of the content of $\alpha$'-martensite near the fracture surface has been carried out, at room temperature, using light optical micrography. All the experiments have been performed at CERN.

*4.1.1. Mechanical tests*

Elastic-plastic fracture toughness tests with fatigue-precracked Compact Samples for the opening mode of loading (i.e. Mode I) have been carried out at liquid nitrogen temperature ($T = 77$ K) and at liquid helium temperature ($T = 4$ K), according to the standard ASTM-E1820-20a (2020). The tests have been used to compute crack-growth resistance $J - R$ curves following the so-called "resistance curve procedure" (see ASTM-E1820-20a (2020)), i.e. using a single Compact Sample to obtain the complete $J - R$ curve. Experiments at room temperature have not been performed. For the two analysed materials, samples with thickness greater than 12 mm (this is the thickness of the plates from which all samples tested in this work are extracted, see Section 2) are needed to obtain fracture toughness values at room temperature that are independent of the sample size. As a reference, the threshold thickness for the AISI 304L is estimated to be around 25.4 mm based on the work of Sa et al. (2005).

The same servo-hydraulic testing machine and cryostat used for the uniaxial tensile tests (Section 3.1.1) have been employed to perform the fatigue pre-cracking and the fracture toughness experiments. The basic design lines of the tension testing clevis were presented by Malik (2021), so that in this work we have just removed the clevis corners (3 mm $\times$ 3 mm) to better accommodate the clip gage (see the following paragraphs), and reduced the loading-pin diameter to 10 mm. Moreover, the design of the Compact Sample consists of an "alternative specimen" according to ASTM-E1823-20a (2020), with a width-to-thickness ratio of $W/B = 4$ ($W = 40$ mm and $B = 10$ mm, see the corresponding dimensions in Fig. 17). The design of the integrated sharp edges has been devised taking into account the clip gage used for the fracture toughness tests. The Compact Samples have been extracted from the mid-thickness of each material plate with the load-line axis parallel to the rolling direction (L-T direction according to the standard ASTM-E1823-20a (2020)). They have been machined using spark-erosion for the in-plane geometry and subsequent milling to obtain the pin holes and the desired thickness.

Fatigue pre-cracking of the Compact Samples has been carried out at room temperature according to the standard ASTM-E1823-20a (2020), following the same procedure for both materials, with the purpose of obtaining a sharp precrack. Monitoring of the precrack has been performed with a portable optical microscope (Wi-Fi Digital Microscope RS PRO 913-2478). In order to have a clear visualization of the progression of the sharp precrack, a manual grinding of the sample's side was performed before. The precrack has been produced by cyclic loading the sample with a sinusoidal waveform at a maximum frequency of 30 Hz under force control using a load ratio of $R = P^f_{max}/P^f_{min} = 0.1$. The first step of the pre-cracking has been conducted using a maximum load of $P^{f(1^{st})}_{max} = 1$ kN, which corresponds to a maximum intensity

factor of $K_{max}^{f(1^{st})} \approx 8$ MPa$\sqrt{\text{m}}$. The transition to the second step has been done when the number of cycles is $\approx 10^5$. For the second step a maximum load of $P_{max}^{f(2^{nd})} = 4$ kN has been selected which corresponds to a maximum intensity factor of $K_{max}^{f(2^{nd})} \approx 35$ MPa$\sqrt{\text{m}}$. The test was stopped at the moment in which the precrack reached approximately 3 mm (from the sharp notch, see Fig. 17), which corresponds to an initial crack size of $a_0 \approx 0.65W \approx 26$ mm (distance from load line to fatigue precrack tip, see Fig. 17). Hence, the remaining ligament is $b_0 = W - a_0 \approx 14$ mm. Next, side grooves with a total thickness reduction of approximately 2 mm ($0.20B$) were machined, so that the sample net thickness in the plane of the precrack is $B_N \approx 8$ mm. The machining has been performed using spark-erosion since, according to Weiss and Nyilas (2006), it leads to a straighter crack front during the fracture toughness test.

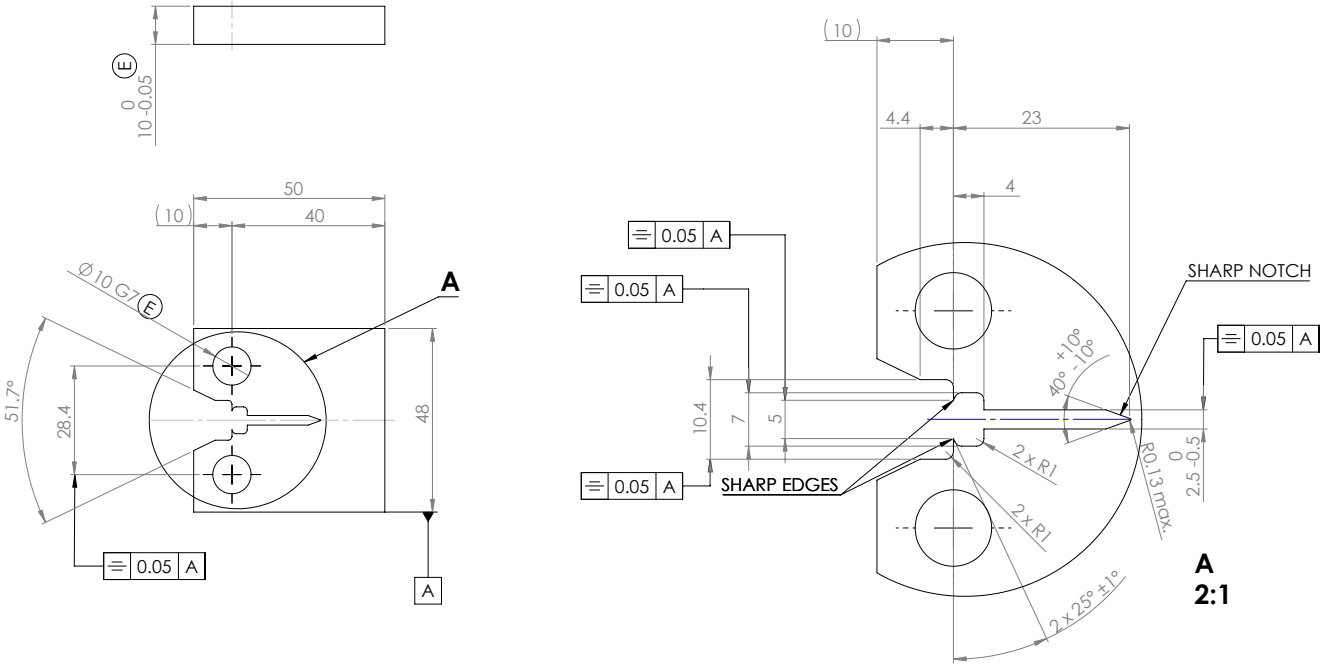


Figure 17: Design of the Compact Sample used in the fracture toughness tests.

The elastic-plastic fracture toughness tests have been performed according to the standard ASTM-E1820-20a (2020), following the "resistance curve procedure" (as mentioned before). The load was applied under displacement control of the machine's cross head at a speed of 0.5 mm/min, and it was measured by the machine's load cell. A number of unloading-reloading sequences have been performed along the test every 0.14 mm ($0.01b_0$) of the machine's cross-head displacement, with a force reduction range of 2 kN ($0.5P_{max}^{f(2^{nd})}$). A cryogenic clip gage (Epsilon 3541-005M-040M-LT), with a gauge length of 5 mm and a measuring range of +4 mm/−1 mm, has been used to measure the load-line displacement. As mentioned before, for all the tests performed the cryogenic test setup described in Section 3.1.1 has been employed. Three fracture toughness tests per material and testing temperature have been conducted. The tests are stopped shortly after the point of maximum force is exceeded, which is an indication that the crack has propagated, and before the clip gage reaches the maximum measuring range of 5 mm. The final crack size after testing has been marked by heat tinting the sample at 400°C for 1 hour. Subsequently, the sample has been fractured in order to analyse the crack. This was

performed by fatigue cracking, aiming at minimizing additional deformation in the sample, using the same procedure employed for the second step of fatigue pre-cracking (see previous paragraph). Identification of the initial and final crack sizes has been conducted using an optical microscope. The initial crack size corresponds to the end of the flat fatigue precracked area, while the final crack size is marked by the colouration from heat tinting (see Fig. 19).

The load and load-line displacement measurements obtained from the fracture toughness experiments have been used to compute the crack-growth resistance $J-R$ curves, which serve to determine the fracture toughness parameters $J_Q$ and $K_{JQ}$. These parameters are qualified as size-independent plane-strain values, $J_{Ic}$ and $K_{JIc}$, provided that they meet the size criteria specified in Sections A9.10.1 and A9.10.2 of the standard ASTM-E1820-20a (2020). As mentioned before, four different methods have been used for the calculation of the $J-R$ curves, which is an original methodological contribution of this paper.

- **ASTM Compliance Method**. The *official* procedure provided by the standard ASTM-E1820-20a (2020) is an elastic-compliance approach based on the assumption that as the crack grows, the sample becomes less stiff, leading to an increase of the unloading compliance with respect to the previous unloading. The crack length is related to the unloading compliance using the equations provided in the Appendix of the standard ASTM-E1820-20a (2020) devoted to the Compact Sample (Appendix 2 - Special requirements for testing compact specimens), which includes an adjustment procedure to improve the estimation of the initial crack size. The adjustment is based on a third-order polynomial regression fitting of crack size versus $J$ values (Section A9.3 therein).

- **W-N Compliance Method**. This approach was developed in the works of Nyilas et al. (1998) and Weiss and Nyilas (2006), and includes two improvements with respect to the ASTM Compliance Method. On the one hand, it proposes a solution for the so-called apparent negative crack extension (a problem not addressed by the ASTM Compliance Method), which results from an experimentally-measured continuously increasing stiffness with respect to previous unloadings at the initial stage of the test (Seok, 2000; Rosenthal et al., 1990; Voss, 1983). While there is not a general consensus about the causes behind the apparent negative crack extension, Nyilas et al. (1998) and Weiss and Nyilas (2006) mainly attributed the initial increase of the sample's stiffness to the strain hardening of the plastic zone ahead of the precrack tip during blunting, which does not imply actual crack growth. Thus, the W-N Compliance Method identifies the crack initiation when the overall stiffness changes from an increasing to a decreasing behaviour, i.e. when the blunted precrack turns into ductile tearing. The data points before the designated crack initiation are not included in the $J-R$ curve, and therefore, no negative crack growth is predicted. On the other hand, the W-N Compliance Method improves the estimation of the crack lengths, replacing the experimentally-measured compliances by the so-called "corrected compliance function" of load-line displacement, which results from the construction of a second-order polynomial regression of stiffness versus displacement at the onset of unloading. The

specific form of the polynomial regression is determined by imposing three conditions: (i) the displacement at the onset of the last unloading is associated with the compliance calculated with the equation (A2.11) of the standard ASTM-E1820-20a (2020) using the measured final crack length, (ii) the displacement at the crack initiation is associated with the compliance calculated with the equation (A2.11) of the standard ASTM-E1820-20a (2020) using the measured initial crack length, and (iii) the maximum of the polynomial regression corresponds with the displacement associated to the crack initiation. Note that the measured initial crack length rather corresponds to the sharp precrack than to the blunted precrack. However, since the sharp precrack is readily measurable using optical microscopy, see Fig. 19, the "corrected compliance function" directly associates the sharp precrack with the crack initiation for the sake of simplicity. Generally, the difference between the blunted precrack and the sharp precrack is between 50 $\mu$m and 400 $\mu$m (Tarafder and Tarafder, 2006). Moreover, the W-N Compliance Method relates the values of $J$ with the improved estimation of the crack extensions and the entire $J-R$ curve is shifted so that the crack initiation point coincides with the "construction line" (also referred to as blunting line). After the shifting, the computed value for the initial crack length is calculated as the crack length corresponding to a crack extension $\Delta a = 0$ (see Fig. 21), which is smaller than the experimental measurement of the initial crack length due to the simplification of associating the sharp precrack with the crack initiation point.

- **Modified W-N Compliance Method**. This approach is an original contribution of this paper, and the main difference with respect to the W-N Compliance Method is that the values of $J$ are re-calculated using the improved estimation of the crack lengths obtained from the "corrected compliance function" of displacement. Moreover, the "corrected compliance function" associates the crack initiation with the blunted precrack, instead of with the sharp precrack, using an iterative procedure. The iterative procedure starts assuming that the blunted precrack is equal to the sharp precrack, the simplification used in the W-N Compliance Method. Once the $J-R$ curve is obtained, instead of performing the shifting to the blunting line, a new estimation of the blunted precrack is calculated as the sum of the measured initial crack length and the ratio between the $J$ value of the current crack initiation point and the slope of the blunting line, indicated in Fig. 18(a). The iterative process is then re-started, so that in each iteration, "corrected compliance function", crack lengths, $J$ values, $J-R$ curve and blunted precrack are updated. The iterative process ends when the difference between current and previous estimation for the blunted precrack is lower than $10^{-5}$ mm, so that this iterative process ensures that the crack initiation point coincides with the blunting line and the computed initial crack length equals the measured initial crack length.

- **ASTM Normalization Method**. The Normalization technique enables direct estimation of the crack lengths from a test performed under continuous displacement increase, so that unloading-reloading sequences are not needed and estimations of intermediate crack lengths are based on the load versus load-line displacement record, as well as on the initial and final measured crack sizes (Herrera and Landes, 1990; Landes et al., 1991; Lee, 1995; Joyce,

2001). The Normalization method which has been used in this work is described in Annex 15 of the standard ASTM-E1820-20a (2020). Since the fracture toughness tests presented in this paper have been performed according to the "resistance curve procedure", the data of the unloading-reloading sequences had to be removed. Specifically, we have retrieved for the analysis the whole record of load and displacement until the onset of the first unloading, one data-point between each unloading sequence, and the point corresponding to the onset of the last unloading.

The code used for construction of the crack-growth resistance $J-R$ curves, and the identification of the fracture toughness parameters $J_Q$ and $K_{JQ}$, is included as *Supplementary Material*.

#### *4.1.2. Martensite measurements*

Light optical micrography inspections have been carried out to investigate the extent of the $\alpha$'-martensitic transformation near the fracture surface of the Compact Samples after testing. The analysis encompasses samples of both materials, AISI 30L and AISI 316LN, tested at 77 K and 4 K. The samples selected for the analysis have been cut into two parts along their mid-thickness plane. One cutting plane for each specimen has been metallographically prepared. The cut and metallographic preparation have been carried out following the same procedure described in the item **Electron backscatter diffraction** of Section 3.1.2. The as-polished state of the surface has been used for the inspection. The micrographs have been acquired with the equipment described in the item **Quantitative light optical micrography** of Section 3.1.2. Stitching images composed by individual micrographs taken at the high magnification of 200 have been obtained in order to have a global image of the distribution of $\alpha$'-martensite. Each stitching covers a region of about 7 mm along the fracture surface and 4 mm below it, see Fig. 20. The stitching's length includes the fracture surface corresponding to the final part of the fatigue pre-cracking and the total length of the crack developed in the fracture toughness tests.

### *4.2. Results*

Fig. 18 shows fracture toughness experimental results for AISI 304L and AISI 316LN. The crack-growth resistance $J-R$ curves are computed with the ASTM Normalization Method. Filled and empty symbols represent data points that fall inside and outside the "Region of Qualified Data", which is determined according to Fig. A9.2 of the standard ASTM-E1820-20a (2020). Large darker symbols indicate the fracture toughness $J_Q$, which is obtained from the intersection of the power law regression line with the "$0.2-$mm offset line" (Section A9.6.6 of the standard ASTM-E1820-20a (2020)). The power law regression line is defined by fitting the expression $J=C_1\Delta a^{C_2}$, where $\Delta a$ is the crack extension and $C_1$ and $C_2$ are constants, to the data that fall into the "Region of Qualified Data", and it is pictured with solid lines in the figure. Dashed lines correspond to the "construction line" (blunting line) and the "$0.2-$mm offset line", as indicated in the graph, with the slope being $2\sigma_Y=\sigma_{YS}+\sigma_{TS}$, according to the standard ASTM-E1820-20a (2020). Results corresponding to three different experiments (i.e., three different realizations for the same material and testing conditions) indicated

with circular, square and triangular symbols are included in each graph. Specifically, Figs. 18(a) and 18(b) picture the results for AISI 304L tested at 77 K and 4 K, respectively, and Fig. 18(c) shows the results for AISI 316LN tested at 4 K. Notice that, in the three graphs, the results obtained with the three realizations are similar, which shows the robustness and repeatability of the measurements. The comparison of results for both materials and testing temperatures shows that the AISI 316LN displays higher fracture toughness than the AISI 304L (check Figs. 18(b) and 18(c)), and for the AISI 304L the fracture toughness decreases with decreasing testing temperature (check Figs. 18(a) and 18(b)). No results for AISI 316LN at 77 K are provided as during the three performed fracture toughness tests the crack did not propagate for displacements within the clip gage measuring range, so that no data points within the "Region of Qualified Data" were obtained. The comparison of the crack-growth resistance $J-R$ curves obtained in this work with data available in the literature is performed in Appendix B.

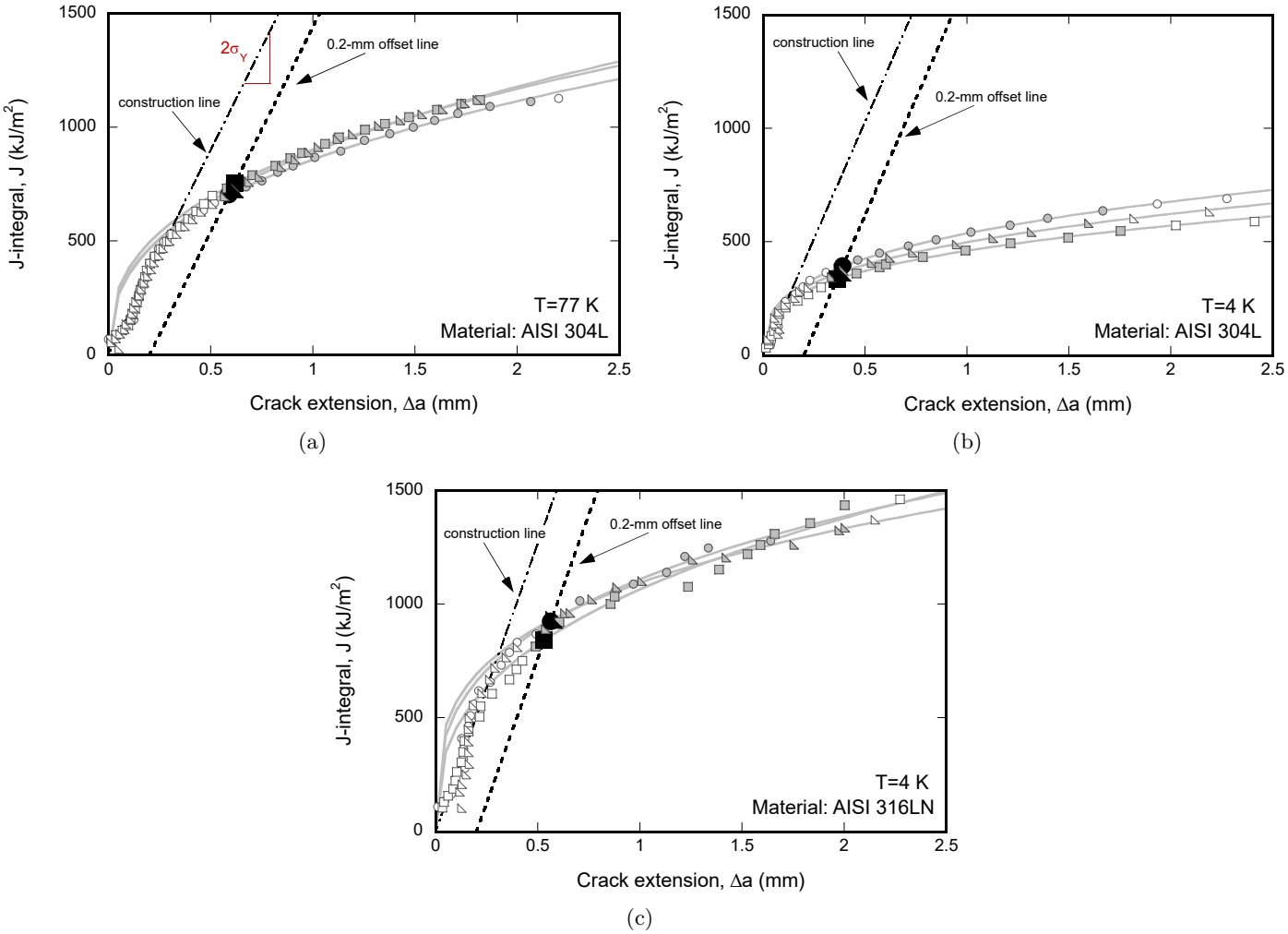


Figure 18: Fracture toughness experimental results for AISI 304L and AISI 316LN. Crack-growth resistance $J-R$ curves computed with the ASTM Normalization Method. Filled and empty symbols represent data points that fall inside and outside the "Region of Qualified Data", respectively. Large darker symbols indicate the fracture toughness $J_Q$. Solid lines represent the power law regression fitting. Dashed lines correspond to the "construction line" (blunting line) and the "$0.2-$mm offset line", as indicated in the graphs. Results corresponding to three different experiments indicated with circular, square and triangular symbols are included in each graph: (a) AISI 304L tested at $T=77$ K, (b) AISI 304L tested at $T=4$ K and (c) AISI 316LN tested at $T=4$ K.

Fig. 19 presents optical micrographs of the fracture surface for experiments performed with AISI 304L tested at 77 K and 4 K, and AISI 316LN at 4 K. The sharp notch, the surface corresponding to the pre-cracking, and the surface corresponding to the fracture toughness test are indicated in the pictures. A close view of the blunting zone is enlarged on the left bottom part of Fig. 19(a). Notice that for the AISI 316LN sample, Fig. 19(c), the blunting is not easily identifiable in the optical micrographs due to the rough and granular appearance of the fracture surface for this material. In the case of AISI 304L, Figs. 19(a)-(b), the crack front presents the so-called tunnelling effect (Weiss and Nyilas, 2006), with much shorter crack extension near the sample's edges. In contrast, notice that for the AISI 316LN sample, the tunnelling effect is less pronounced. On the other hand, irrespective of the different crack front shapes, the crack front of all tested samples fulfils the requirements of the standard ASTM-E1820-20a (2020) (see Sections 9.1.4.1, 9.1.4.2 and 9.1.5.1). Moreover, the optical micrographs make evident the formation of a neck in the samples –pointed out in the pictures– that leads to a reduction of thickness of $\approx 5.5\%$, $\approx 3\%$ and $5\%$ for AISI 304L tested at 77 K, AISI 304L at 4 K and AISI 316LN at 4 K, respectively.

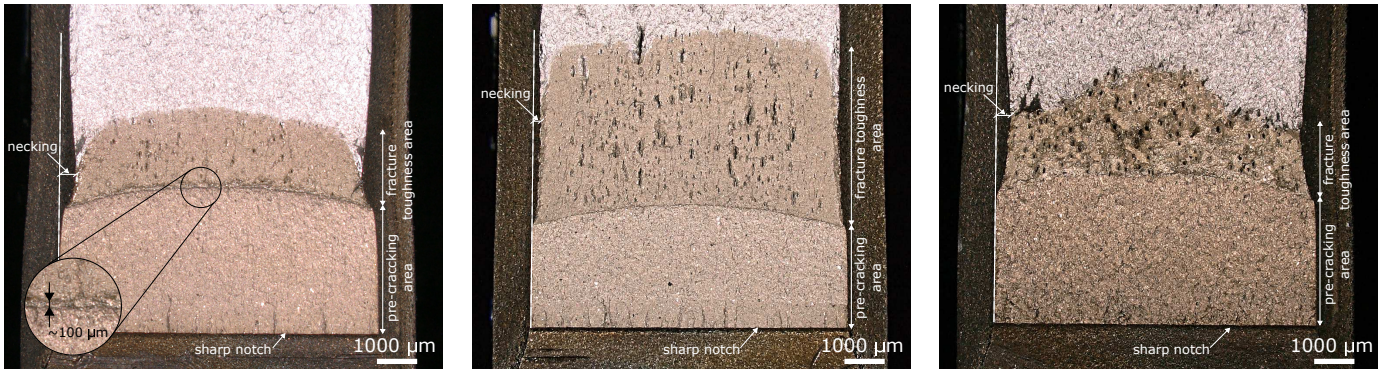


(a) (b) (c)

Figure 19: Optical micrographs of the fracture surface for: (a) AISI 304L tested at $T = 77$ K, (b) AISI 304L tested at $T = 4$ K and (c) AISI 316LN tested at $T = 4$ K. The neck, the sharp notch, the surface corresponding to the pre-cracking, and the surface corresponding to the fracture toughness tests are indicated in the pictures.

Fig. 20 shows stitched micrographs obtained by light optical microscopy of the fractured samples near the fracture surface, for the same samples investigated in Fig. 19. The surfaces corresponding to the pre-cracking and the fracture toughness test are indicated in the pictures. A close view of the fracture toughness area is enlarged on the bottom part of the images in order to illustrate the lath-type $\alpha'$-martensite morphology. Note that the martensite appears in black, and the austenite in grey, as indicated in the legend located in the bottom left part of the micrographs. The highest concentration of martensite is located next to the fracture surface, decreasing towards the bulk, most likely due to decreasing plastic strain. The content of martensite seems to be greater in the AISI 304L samples, which is consistent with the results reported in Figs. 15 and 16 of Section 3.2, which showed that the martensitic transformation is faster

and more important in AISI 304L than in AISI 316LN. Note that for AISI 304L, more martensite is observed in the sample tested at 77 K, most likely because the plastic deformation near the crack is greater than at 4 K. Furthermore, the AISI 304L samples show more regular and plane crack path, with decreased fracture surface roughness, in comparison with the results obtained with AISI 316LN, as anticipated in Fig. 19. This can be attributed to the higher amount of the martensitic phase shown by the AISI 304L specimens (the martensite being less ductile than the austenite).

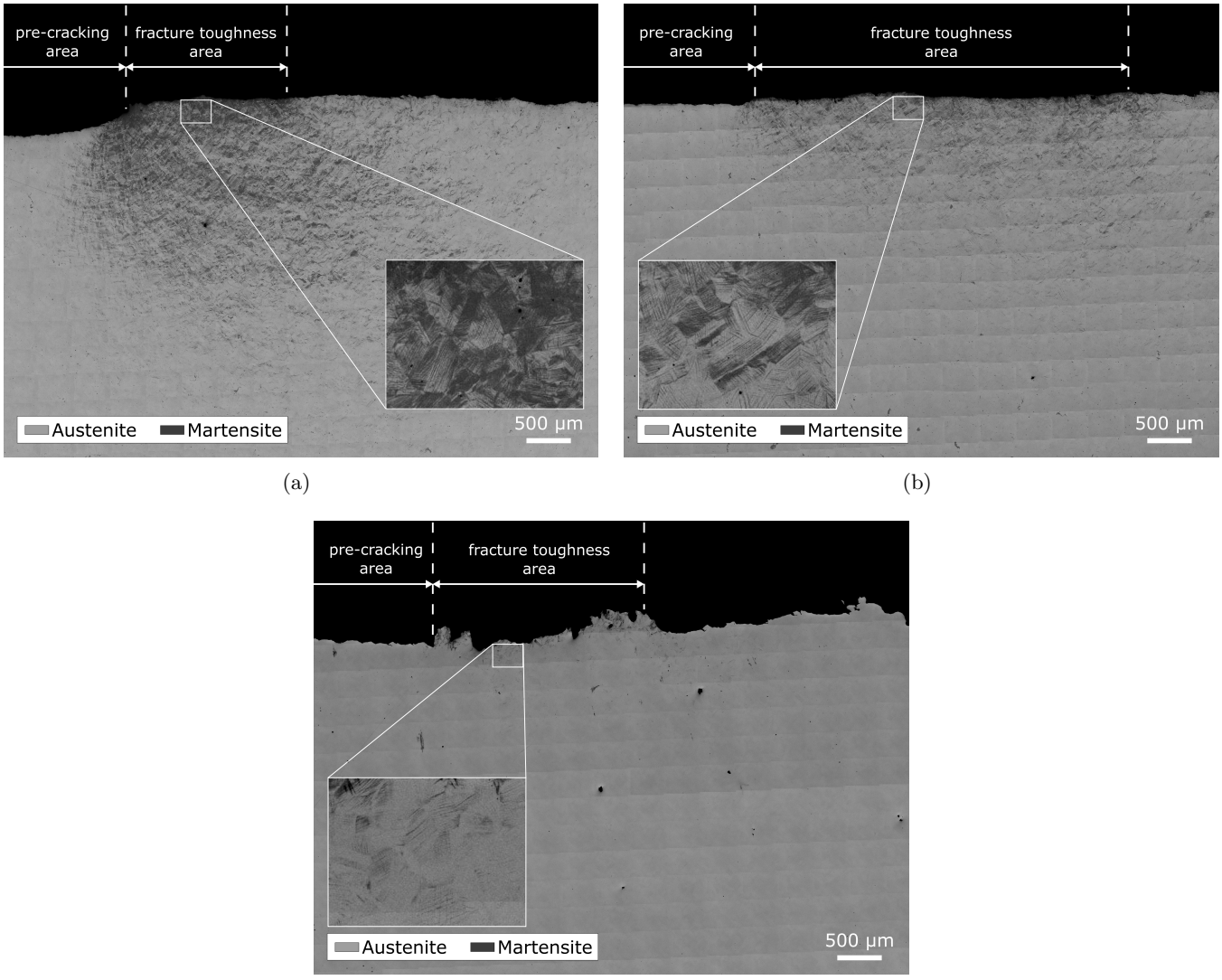


Figure 20: Stitched micrographs obtained by light optical microscopy of the fractured specimens near the fracture surface. (a) AISI 304L tested at $T = 77$ K, (b) AISI 304L tested at $T = 4$ K and (c) AISI 316LN tested at $T = 4$ K.

The comparison between the results obtained with the four approaches described in Section 4.1 to compute the crack-growth resistance $J-R$ curves (ASTM Compliance Method, W-N Compliance Method, Modified W-N Compliance Method and ASTM Normalization Method) is performed in Fig. 21. As in Fig. 18, filled and empty symbols represent data points that fall inside and outside the "Region of Qualified Data", respectively. Large darker symbols indicate the

fracture toughness $J_Q$; the power law regression fitting being represented by solid lines. Each colour corresponds to the results obtained with a given method, see the legend in the bottom right part of the graph. Moreover, dashed lines correspond to the "construction line" (blunting line) and the "$0.2-$mm offset line". There are noticeable differences between the crack-growth resistance $J-R$ curves obtained with the four different methods. For instance, while the values of $J$ computed with the Modified W-N Compliance Method and the ASTM Normalization Method are similar, they lie above the data obtained with the W-N Compliance Method. Moreover, note that, in comparison with the other three approaches, the ASTM Compliance Method greatly underestimates the value of $J_Q$: the negative crack extension causes two points with $J \approx 0$ to fall into the "Region of Qualified Data" so that the power law regression line does not properly represent the $J-R$ evolution obtained for most of the data points.

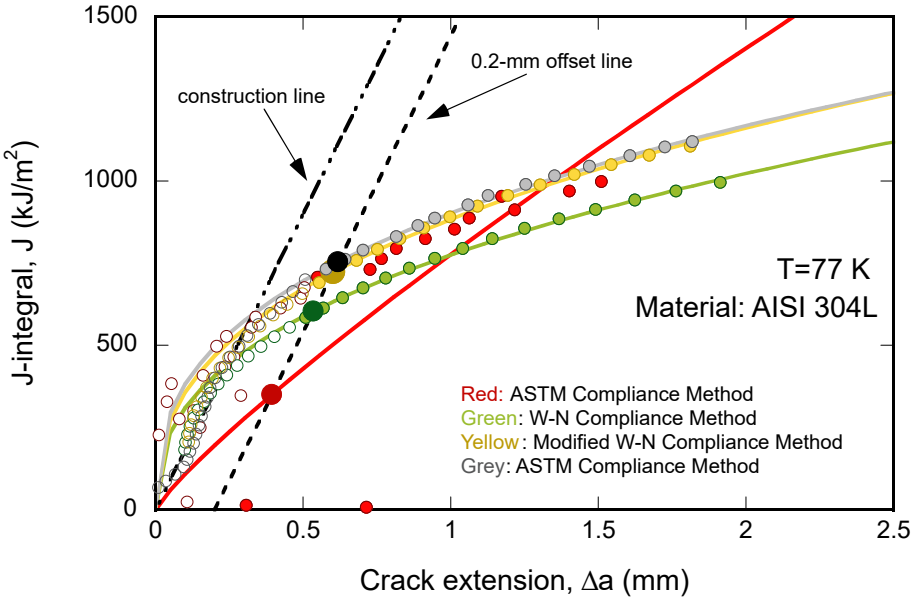


Figure 21: Fracture toughness experimental results for AISI 304L tested at $T = 77$ K. Crack-growth resistance $J-R$ curves computed with the four approaches described in Section 4.1: ASTM Compliance Method, W-N Compliance Method, Modified W-N Compliance Method and ASTM Normalization Method. Filled and empty symbols represent data points that fall inside and outside the 'Region of Qualified Data", respectively. Large darker symbols indicate the fracture toughness $J_Q$. Solid lines representing the power law regression fitting. Each colour corresponds to the results obtained with a given method. Dashed lines correspond to the "construction line" and the "$0.2-$mm offset line". To be noted the incorrect determination of the pseudo fracture toughness $J_Q$ with the ASTM Compliance Method due to the negative crack extension which causes two points with $J \approx 0$ to fall in the 'Region of Qualified Data".

Additional quantitative comparison between the results obtained with the four approaches used to compute the $J-R$ curves is provided in Table. 4. The intensity factor $K_{JQ} = \sqrt{\dfrac{E\,J_Q}{1-\nu^2}}$, where $E = 206$ GPa and $\nu = 0.3$ are the Young's modulus and the Poisson's ratio, respectively, is calculated for AISI 304L at 77 K and 4 K, and for AISI 316LN at 4 K, for the three experiments performed per material-temperature combination. Notice that for some experiments the tests data do not fulfil the requirements established by the standard for $K_{JQ}$ to be considered the actual intensity factor. To be highlighted that if $K_{JQ}$ is the actual intensity factor (i.e. it fulfils all the requirements of the standard), we have that $K_{JQ} = K_{JIc}$ (size-independent plane-strain intensity factor), since the size criteria, $B > 10J_Q/\sigma_Y$ and

$b_0 > 10J_Q/\sigma_Y$ according to Sections A9.10.1 and A9.10.2 of the standard ASTM-E1820-20a (2020)), are fulfilled for all the tests performed in this work.

For instance, none of the $K_{JQ}$ values which have been obtained using the ASTM Compliance Method fulfil all the requirements listed in ASTM-E1820-20a (2020) because the qualification requirements included in Sections A9.3.3.2, A9.4 and 9.1.5.2 and Note A9.1 are repeatedly breached. Note A9.1 indicates that *anomalies* at the beginning of the test, due to the apparent negative crack extension in the experiments performed in this work, cause points with low $J$ to fall within the "Region of Qualified Data", providing an unreasonable low value of $K_{JQ}$ (where Note A9.1 is mentioned in Table 4, the resulting $K_{JQ}$ value is not included as it is not consistent with the corresponding $J-R$ curve, see Fig. 21). Furthermore, since the ASTM Compliance Method does not address the negative crack extension phenomenon, see the item **ASTM Compliance Method** in Section 4.1.1, the adjustment procedure to obtain an improved estimation of the initial crack size is not effective to evaluate the data obtained from most tests. Specifically, the correlation coefficient of the data which resulted from the adjustment procedure is lower than 0.96, so that the test data are invalid according to Section A9.3.3.2 of ASTM-E1820-20a (2020). In addition, for some tests the adjustment procedure underestimates the initial crack size by more than 0.5 mm with respect to the measurements obtained with optical microscopy, making the result invalid according to Section A9.4 of ASTM-E1820-20a (2020). The large difference between estimated and measured initial crack size is most likely due to the defective estimation of the crack size using the compliance equations rather than a consequence of the adjustment procedure, so that for some of the experiments the difference between predicted and measured crack extension is larger than the maximum value accepted in Section 9.1.5.2 of ASTM-E1820-20a (2020).

In contrast, the W-N Compliance Method addresses the problem related to the negative crack extension and corrects the estimation of the crack lengths, see the item **W-N Compliance Method** in Section 4.1.1. Furthermore, despite the estimation of the initial crack length does not match with the measurement obtained with optical microscopy, the difference is lower than 200 $\mu$m, what is acceptable within the standard ASTM-E1820-20a (2020), so that the values of $K_{JQ}$ qualify as $K_{JIc}$.

For the Modified W-N Compliance Method all the resulting $K_{JQ}$ values also qualify as $K_{JIc}$. The quantitative differences with the results obtained with the W-N Compliance Method –which yields lower values for $K_{JQ}$– are most likely due to the re-calculation of the values of $J$ using the improved values of the crack sizes, see the item **Modified W-N Compliance Method** in Section 4.1.1. Moreover, the iterative process implemented for the estimation of the crack sizes predicts that the crack extension caused by blunting is approximately 100 $\mu$m, 30 $\mu$m and 80 $\mu$m for AISI 304L at 77 K, AISI 304L at 4 K and AISI 316LN at 4 K, respectively. Note that the predictions for AISI 304L find reasonable agreement with the experimental measurements presented in Fig. 19 (recall that the crack extension caused by blunting could not be measured for AISI 316LN).

Regarding the ASTM Normalization Method, some of the tests do not comply with the additional restriction included

in Section A15.2.4 of the standard ASTM-E1820-20a (2020) which states that the measured crack extension should not exceed the lesser of 4 mm or 15% of the initial uncracked ligament. Nonetheless, the other additional requirements included in the standard are met, so that the values of the intensity factor obtained from the tests are assumed to qualify as $K_{JIc}$. Furthermore, while this approach does not require to carry out a series of unloading-reloading sequences during the fracture toughness tests, which makes the ASTM Normalization Method more sound and practical to analyse compared to the other three compliance methods, see the item **ASTM Normalization Method** in Section 4.1.1, the results obtained for $K_{JQ}$ are very similar, qualitatively and quantitatively, to the ones computed with the Modified W-N Compliance Method. This also suggests that breaching the additional requirement included in Section A15.2.4 of the standard ASTM-E1820-20a (2020) does not have an important influence for the determination of $K_{JQ}$.

| | ASTM Compliance Method | | W-N Compliance Method | | Modified W-N Compliance Method | | ASTM Normalization Method | |
|---|---|---|---|---|---|---|---|---|
| | $K_{JQ}$ (MPa$\sqrt{\text{m}}$) | Invalid requirements | $K_{JQ}$ (MPa$\sqrt{\text{m}}$) | Invalid requirements | $K_{JQ}$ (MPa$\sqrt{\text{m}}$) | Invalid requirements | $K_{JQ}$ (MPa$\sqrt{\text{m}}$) | Invalid requirements |
| **AISI 304L T = 77 K** | 385.56 | Section A9.3.3.2<br>Section A9.4<br>Section 9.1.5.2 | 348.62 | - | 389.60 | - | 399.04 | - |
| | - | Section A9.3.3.2<br>Section A9.4<br>Section 9.1.5.2<br>Note A9.1 | 369.87 | - | 404.71 | - | 413.11 | - |
| | 367.57 | Section A9.4<br>Section 9.1.5.2 | 353.43 | - | 393.06 | - | 405.93 | - |
| **AISI 304L T = 4 K** | - | Section A9.3.3.2<br>Section A9.4<br>Section 9.1.5.2<br>Note A9.1 | 273.31 | - | 286.37 | - | 298.03 | Section A15.2.4 |
| | 264.46 | Section A9.3.3.2 | 247.41 | - | 251.11 | - | 276.21 | Section A15.2.4 |
| | - | Section A9.3.3.2<br>Note A9.1 | 270.34 | - | 272.82 | - | 287.19 | Section A15.2.4 |
| **AISI 316LN T = 4 K** | - | Section A9.3.3.2<br>Section A9.4<br>Section 9.1.5.2<br>Note A9.1 | 414.35 | - | 434.23 | - | 456.89 | - |
| | - | Section A9.3.3.2<br>Section A9.4<br>Note A9.1 | 425.93 | - | 444.84 | - | 436.66 | Section A15.2.4 |
| | - | Section A9.3.3.2<br>Section A9.4<br>Note A9.1 | 419.20 | - | 448.35 | - | 458.97 | - |

Table 4: Intensity factor $K_{JQ}$ results obtained from the fracture toughness tests (three experiments per material-temperature combination) with the four approaches described in Section 4.1 to compute the crack-growth resistance $J-R$ curves: ASTM Compliance Method, W-N Compliance Method, Modified W-N Compliance Method and ASTM Normalization Method. The requirements of the standard that are not met are indicated for each test.

## 5. Concluding remarks

In this paper, we have performed a comprehensive experimental characterization of the microstructural evolution and the mechanical behaviour and fracture of AISI 304L and AISI 316LN austenitic stainless steels at cryogenic temperatures. For that purpose, we have devised an experimental methodology which includes uniaxial tensile experiments and Mode I fracture tests on liquid nitrogen (77 K) and liquid helium (4 K).

We have shown that both AISI 304L and AISI 316LN display a significant increase of the flow stress with decreasing testing temperature and discontinuous plastic flow at 4 K. On the other hand, while the AISI 316LN retains quasi-linear strain hardening and large ductility at cryogenic temperatures, the stress-strain characteristic of the AISI 304L displays a sigmoidal shape and a drop in ductility of nearly 50% as compared to room temperature. The obtained stress-strain curves are in good agreement with results obtained from the literature. Post-mortem microstructural analysis of the tensile samples using magnetic induction, electron backscatter diffraction and quantitative light optical micrography allowed to determine the evolution of the martensitic transformation with the strain. The code developed for the determination of the content of martensite from light optical micrographs is included as *Supplementary Material*. The results obtained with the three methods show the same general trends and reasonable quantitative agreement, bringing out that the martensitic transformation in AISI 304L occurs faster and to a greater extent than in AISI 316LN both at 77 K and at 4 K. The results are in good agreement with the experimental data available in the literature. In addition, the experimental data for the strain-induced martensite fraction have been used to identify the temperature-dependent parameters of the transformation kinetic models proposed by Olson and Cohen (1975) and Garion and Skoczeń (2002).

Moreover, the fracture tests data have been used to determine the crack-growth resistance $J-R$ curves and the fracture toughness of the investigated materials using four different methods here referred to as ASTM Compliance Method, W-N Compliance Method, Modified W-N Compliance Method and ASTM Normalization Method. Out of these four approaches, only the $J-R$ curves computed with the W-N Compliance Method and the Modified W-N Compliance Method fulfil all the requirements of the standard ASTM-E1820-20a (2020) so that the calculated fracture toughness can be considered a material property. On the other hand, note that the results obtained with ASTM Normalization Method are very similar to the crack-growth resistance curves and the fracture toughness computed with the Modified W-N Compliance Method, the main advantage of the ASTM Normalization Method being the simpler procedures required for the test performance and the analysis of test data. The codes developed for the construction of the crack-growth resistance $J-R$ curves, and the identification of the fracture toughness are included as *Supplementary Material*. The experiments have shown that the AISI 316LN has higher fracture toughness than the AISI 304L, and for the AISI 304L the fracture toughness decreases with decreasing testing temperature. The results are in good agreement with the experimental data available in the literature. In addition, post-mortem optical micrography examination of the fracture samples has shown that the amount of austenite transformed into martensite near the fracture surface is greater for AISI 304L than for

AISI 316LN. On the other hand, for AISI 304L there is more martensite formed in the sample tested at 77 K because the plastic deformation near the crack is greater than at 4 K.

**Acknowledgements**

The authors would like to thank A. Gallifa-Terricabras (CERN) for performing the analysis with Digital Image Correlation and A. T. Pérez-Fontenla (CERN) for the help with the SEM imaging. Thanks are also owed to K. Weiss (KIT) for the helpful discussions about fracture toughness.

The research leading to these results has received funding from the European Union's Horizon2020 Programme (Excellent Science, Marie Skłodowska-Curie Actions) under REA grant agreement 777896 (Project QUANTIFY).

## Appendix A. Flow behaviour: comparison with experimental data available in the literature

Figs. A.22 and A.23 show a comparison between the stress-strain curves obtained in this work for AISI 304L and AISI 316LN, and results for the same grades available in the literature, with chemical composition given in Table A.5. Note that all the experimental data for AISI 304L and AISI 316LN available in the literature showed discontinuous plastic flow at 4 K, however, we just display the upper envelop in Figs. 22(c) and 23(c) to facilitate the comparison of results. Generally, there is good qualitative and quantitative agreement between the stress-strain characteristics obtained in this work, and the experimental evidence used for comparison.

Fig. A.24 shows a comparison between the results for the evolution of the volume fraction of martensite $f^{\alpha'}$ with strain $\varepsilon$ obtained in this work and experimental data available in the literature for tests performed at 300 K and 77 K, for the same steel grades, with chemical composition given in Table A.5. Generally, there is good qualitative and quantitative agreement between the results obtained in this work, and the experimental evidence used for comparison. However, no results are available in the literature for AISI 304L and AISI 316LN samples tested at 4 K so that we could compare the martensite volume fraction measurements presented in this paper. No graph is included for the AISI 316LN tested at room temperature because, in agreement with other authors, see Botshekan et al. (1998) and Pattanayak (1984), the martensitic transformation is negligible.

## Appendix B. Fracture behaviour: comparison with experimental data available in the literature

Figs. B.25 shows a comparison between crack-growth resistance $J-R$ curves computed in this paper with the ASTM Normalization Method and experimental results taken from the works of Lee et al. (1998), Murase et al. (1993) and Nyilas and Yanagi (1989). For the experiments performed in this work filled and empty symbols representing data points that

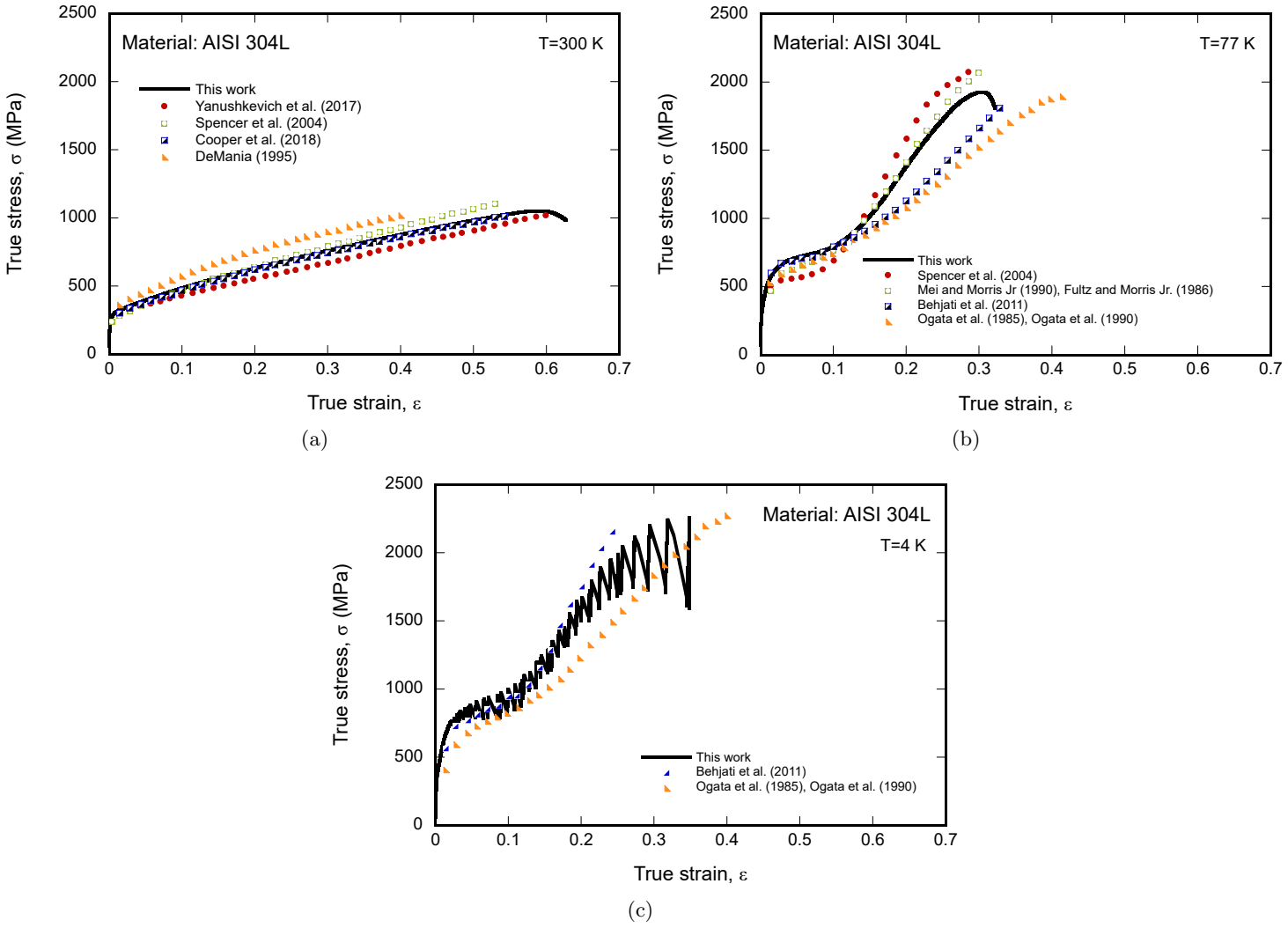


Figure A.22: Comparison between the stress-strain curves obtained in this paper for AISI 304L and experimental results taken from the works of Yanushkevich et al. (2017), Spencer et al. (2004), Cooper et al. (2018), DeMania (1995), Mei and Morris Jr (1990), Fultz and Morris Jr (1986), Behjati et al. (2011), Ogata et al. (1985) and Ogata et al. (1990). Data corresponding to tensile samples tested under quasi-static loading at different temperatures: (a) $T = 300$ K, (b) $T = 77$ K and (c) $T = 4$ K.

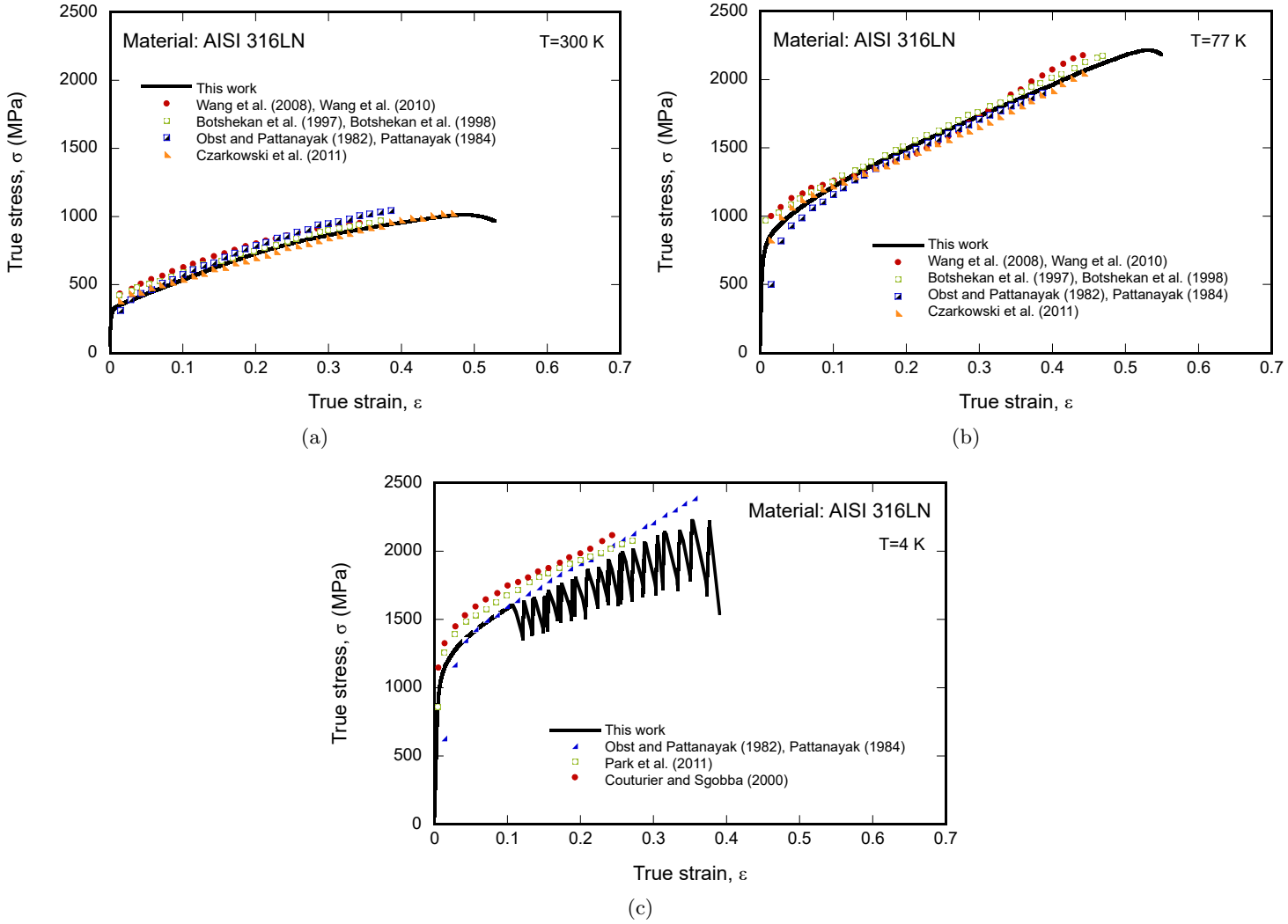


Figure A.23: Comparison between the stress-strain curves obtained in this paper for AISI 316LN and experimental results taken from the works of Wang et al. (2008), Wang et al. (2010), Botshekan et al. (1997), Botshekan et al. (1998), Obst and Pattanayak (1982), Pattanayak (1984), Czarkowski et al. (2011), Park et al. (2011) and Couturier and Sgobba (2000). Data corresponding to tensile samples tested under quasi-static loading at different temperatures: (a) $T = 300$ K, (b) $T = 77$ K and (c) $T = 4$ K.

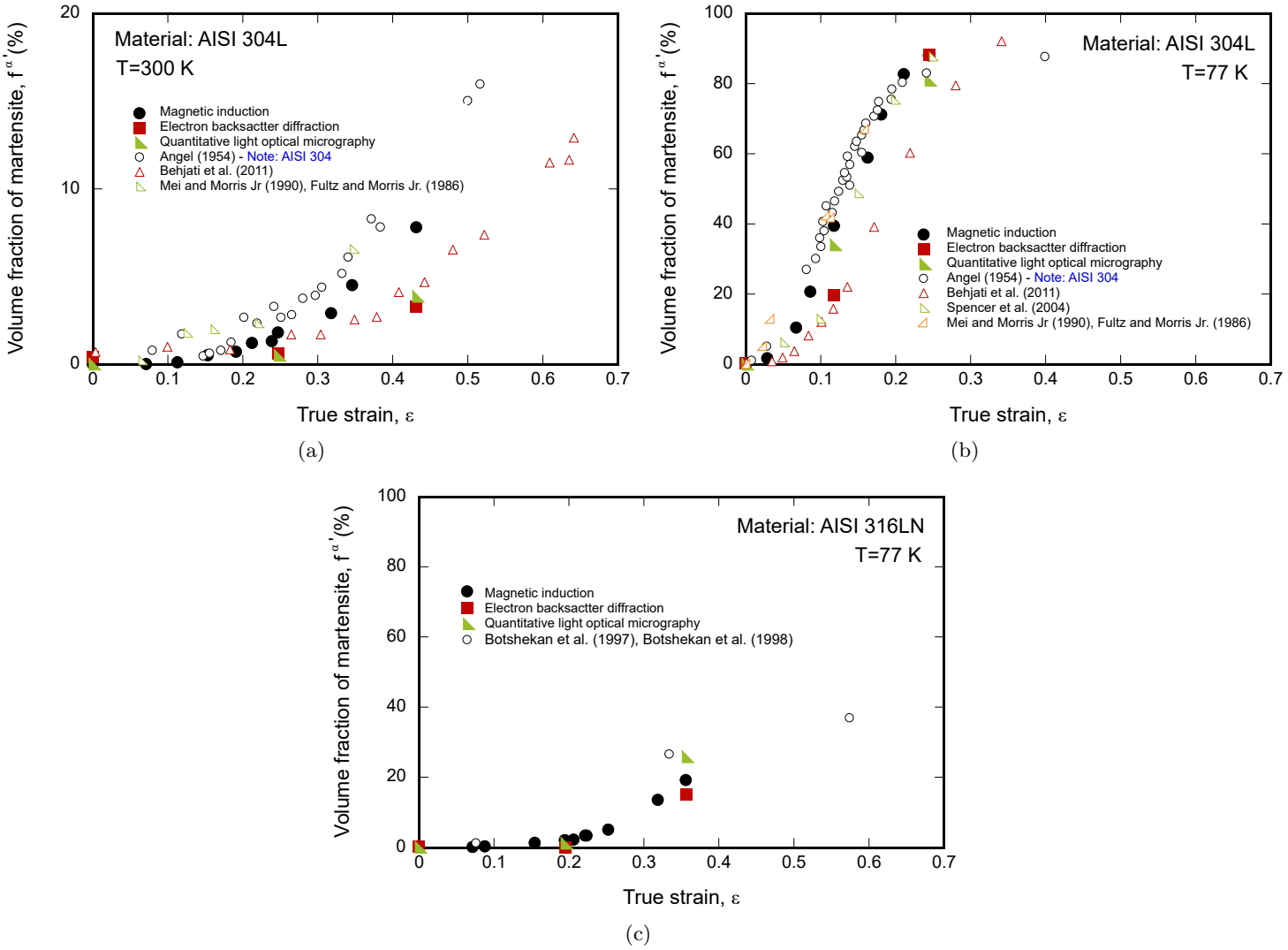


Figure A.24: Comparison between the evolution of the volume fraction of martensite $f^{\alpha'}$ with strain $\varepsilon$ obtained in this paper and experimental results taken from the works of Angel (1954), Behjati et al. (2011), Fultz and Morris Jr (1986), Mei and Morris Jr (1990), Spencer et al. (2004), Botshekan et al. (1997) and Botshekan et al. (1998). Data corresponding to tensile samples tested under quasi-static loading: (a) AISI 304L tested at $T = 300$ K, (b) AISI 304L tested at $T = 77$ K and (c) AISI 316LN tested at $T = 77$ K.

| AISI 304L | | | | | | | | | | | | |
|---|---|---|---|---|---|---|---|---|---|---|---|---|
| **Source** | **C** | **S** | **N** | **Cr** | **Ni** | **Mn** | **Si** | **Mo** | **P** | **Co** | **Cu** | **Nb** |
| Yanushkevich et al. (2017) | 0.04 | 0.04 | - | 18.20 | 8.80 | 1.70 | - | - | 0.05 | - | 0.50 | 0.05 |
| Spencer et al. (2004) | 0.02 | - | 0.07 | 18.22 | 9.03 | 1.85 | 0.56 | 0.34 | - | 0.13 | 0.35 | - |
| Cooper et al. (2018) | 0.03 | - | - | 19.40 | 9.65 | 1.65 | 0.57 | 0.35 | - | - | - | - |
| DeMania (1995) | 0.02 | - | 0.04 | 18.37 | 9.31 | 1.39 | 0.42 | 0.35 | 0.02 | - | 0.39 | - |
| Mei and Morris Jr (1990) | 0.02 | 0.01 | 0.07 | 18.70 | 8.64 | 1.63 | 0.51 | - | 0.02 | - | - | - |
| Fultz and Morris Jr (1986) | | | | | | | | | | | | |
| Behjati et al. (2011) | 0.03 | 0.03 | - | 18.00 | 10.00 | 2.00 | 1.00 | - | 0.04 | - | - | - |
| Ogata et al. (1985) | 0.02 | 0.01 | - | 18.24 | 10.03 | 1.52 | 0.67 | - | 0.03 | - | - | - |
| Ogata et al. (1990) | | | | | | | | | | | | |
| **AISI 316LN** | | | | | | | | | | | | |
| **Source** | **C** | **S** | **N** | **Cr** | **Ni** | **Mn** | **Si** | **Mo** | **P** | **Co** | **Cu** | **Nb** |
| Wang et al. (2008) | 0.01 | - | 0.14 | 15.30 | 12.54 | 1.48 | 0.21 | 2.50 | 0.01 | - | - | - |
| Wang et al. (2010) | | | | | | | | | | | | |
| Botshekan et al. (1997) | 0.03 | 0.03 | 0.16 | 17.2 | 13.5 | 2.00 | 1.00 | 2.50 | 0.05 | - | - | - |
| Botshekan et al. (1998) | | | | | | | | | | | | |
| Obst and Pattanayak (1982) | 0.03 | 0.02 | 0.16 | 16.70 | 13.70 | 1.26 | 0.41 | 2.68 | 0.02 | - | - | - |
| Pattanayak (1984) | | | | | | | | | | | | |
| Czarkowski et al. (2011) | 0.02 | 0.01 | 0.15 | 17.10 | 12.60 | 1.15 | 0.53 | 2.66 | 0.07 | - | 0.16 | - |
| Park et al. (2011) | 0.01 | - | 0.16 | 17.27 | 13.55 | 1.70 | 0.15 | 2.56 | 0.02 | 0.02 | - | - |
| Couturier and Sgobba (2000) | 0.02 | - | 0.16 | 17.33 | 13.03 | 1.26 | 0.61 | 2.61 | 0.03 | - | - | - |

Table A.5: Data source and chemical composition of the reference materials presented in Fig. A.22, A.23 and A.24 (weight-%, Fe balance).

fall inside and outside the "Region of Qualified Data", respectively, large darker symbols indicate the fracture toughness $J_Q$, solid lines represent the power law regression fitting, and dashed lines correspond to the "construction line" and the "$0.2-$mm offset line". Data are shown for AISI 304L tested at 77 K and 4 K in Figs. 25(a) and 25(b), respectively, and for AISI 316LN tested at 4 K in Fig. 25(c). There is qualitative agreement between the experimental results obtained in this work and the data available in the literature –higher fracture toughness for the AISI 316LN, and decreasing fracture toughness with decreasing testing temperature for the AISI 304L–, and also quantitative agreement for the AISI 304L tested at 4 K and for the AISI 316LN tested at 4 K.

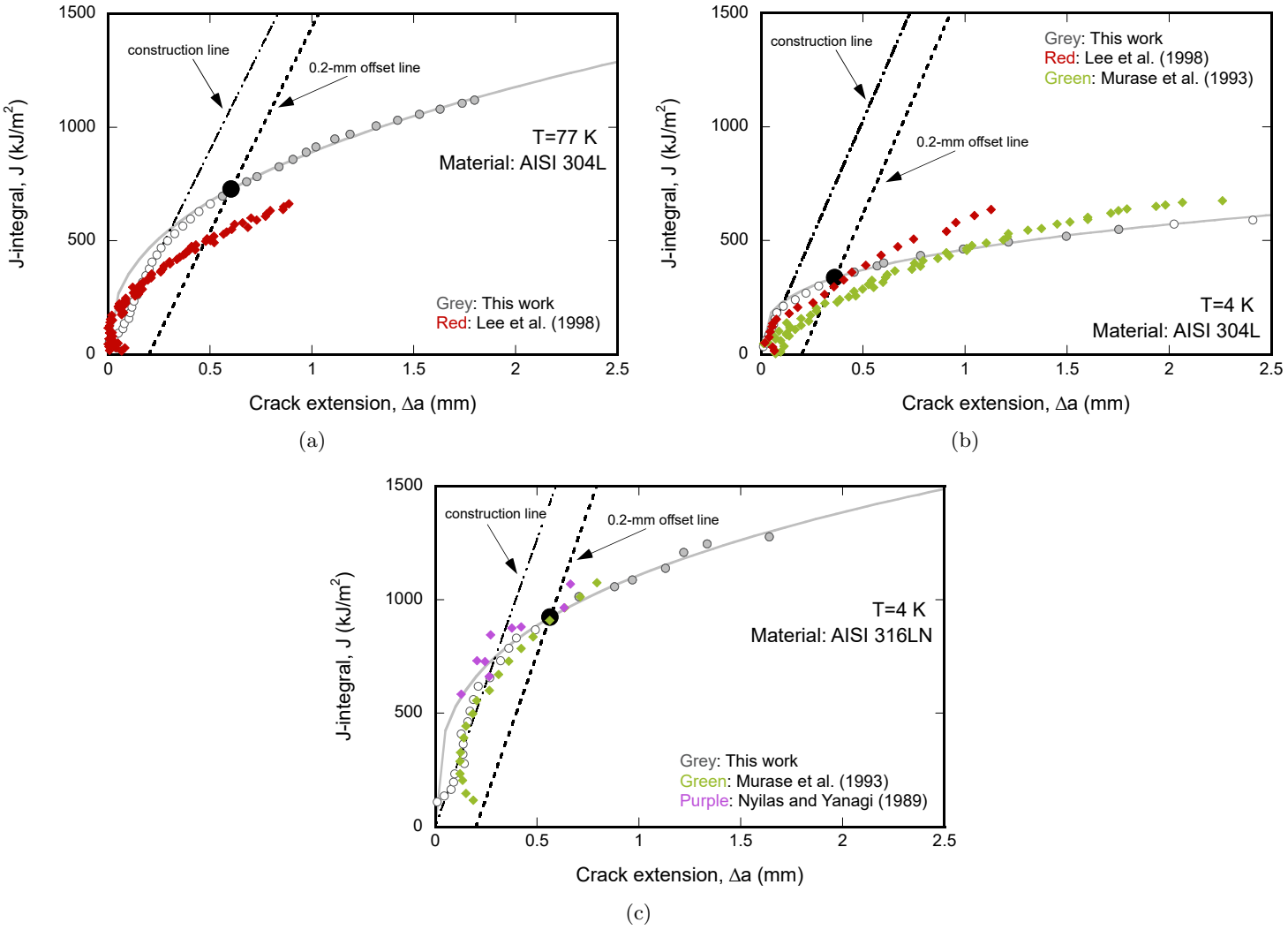


Figure B.25: Comparison between crack-growth resistance $J-R$ curves computed in this paper with the ASTM Normalization Method and experimental results taken from the works of Lee et al. (1998), Murase et al. (1993) and Nyilas and Yanagi (1989). For the experiments performed in this work filled and empty symbols represent data points that fall inside and outside the "Region of Qualified Data", respectively, large darker symbols indicate the fracture toughness $J_Q$, solid lines represent the power law regression fitting, and dashed lines correspond to the "construction line" and the "$0.2-$mm offset line". Data corresponding to fracture toughness tests: (a) AISI 304L tested at $T=77$ K, (b) AISI 304L tested at $T=4$ K and (c) AISI 316LN tested at $T=4$ K.

Fig. B.26 shows the evolution of the fracture toughness $K_{JIc}$ with the initial 0.2% offset yield strength of the material $\sigma_{YS}$ for the tests presented in this paper (solid markers). The experimental results are compared with data available in

| AISI 304L | | | | | | | | | | | | |
|---|---|---|---|---|---|---|---|---|---|---|---|---|
| **Source** | **C** | **S** | **N** | **Cr** | **Ni** | **Mn** | **Si** | **Mo** | **P** | **Co** | **Cu** | **Nb** |
| Lee et al. (1998) | 0.01 | - | - | 18.22 | 9.15 | 1.19 | 0.42 | - | 0.03 | - | - | - |
| Murase et al. (1993) | 0.02 | - | - | 18.36 | 9.67 | 0.82 | - | - | - | - | - | - |
| **AISI 316LN** | | | | | | | | | | | | |
| **Source** | **C** | **S** | **N** | **Cr** | **Ni** | **Mn** | **Si** | **Mo** | **P** | **Co** | **Cu** | **Nb** |
| Murase et al. (1993) | 0.02 | - | 0.18 | 17.88 | 11.16 | 0.84 | - | 2.62 | - | - | - | - |
| Nyilas and Yanagi (1989) | 0.02 | 0.02 | 0.17 | 17.60 | 12.60 | 1.60 | 0.24 | 3.03 | 0.03 | - | - | - |

Table B.6: Data source and chemical composition of the reference materials presented in Fig. B.25 (weight-%, Fe balance).

the literature for AISI 304L and AISI 316LN tested at 77 K and 4 K, and with the NIST trend line for 300 series austenitic stainless steels at 4 K taken from McRae et al. (2017). The general trend is that the fracture toughness decreases as the yield strength of the material increases, the data obtained in this paper being in reasonable qualitative agreement with the experiments taken from the literature.

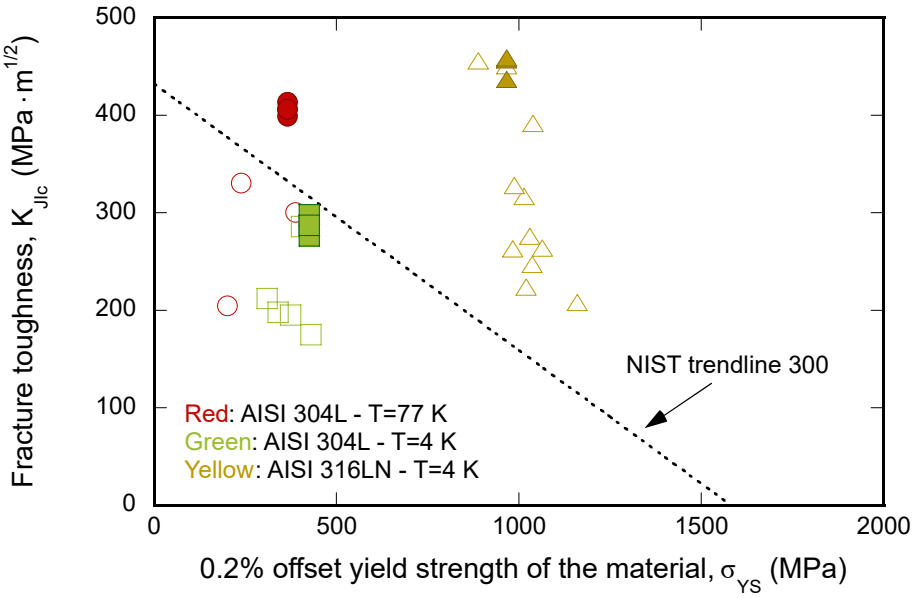


Figure B.26: Fracture toughness $K_{JIc}$ versus 0.2% offset yield strength of the material $\sigma_{YS}$. Comparison of the results obtained in this work for AISI 304L and AISI 316LN with experimental data taken from the works of Shimada et al. (1987), Lee et al. (1998), Purtscher and Read (1987), Park et al. (2019), Morris Jr et al. (1992), Murase et al. (1993), Nyilas and Mitterbacher (2010), Chan et al. (1994), Drexler et al. (1994), Krauth and Nyilas (1980), Mazandarany et al. (1980), Muster and Elster (1990), Nyilas and Yanagi (1989) and Ogata et al. (1992). The experiments taken from the literature and the results obtained in this work are represented with empty and filled symbols, respectively. The dashed line corresponds to the NIST trend line for 300 series austenitic stainless steels at 4 K, taken from McRae et al. (2017).

## References

Angel, T., 1954. Formation of martensite in austenitic stainless steels. Journal of the Iron Steel Institute 177, 165–74.

Apollinari, G., Béjar Alonso, I., Brüning, O., Lamont, M., Rossi, L., 2015. High-Luminosity Large Hadron Collider (HL-LHC): Preliminary design report. Technical Report. CERN, Switzerland.

748 ASTM-A370-15, 2015. Standard Test Methods and Definitions for Mechanical Testing of Steel Products.

749 ASTM-E112-13, 2013. Standard Test Methods for Determining Average Grain Size.

750 ASTM-E1820-20a, 2020. Standard Test Method for Measurement of Fracture Toughness.

751 ASTM-E1823-20a, 2020. Standard Terminology Relating to Fatigue and Fracture Testing.

752 ASTM-E407-07, 2015. Standard practice for microetching metals and alloys.

753 ASTM-E8/E8M-15a, 2015. Standard Test Methods for Tension Testing of Metallic Materials.

754 Avilés-Santillana, I., Betemps, R., Gerardin, A., Guinchard, M., Langeslag, S.A.E., Sgobba, S., 2015. Design and fab-
755 rication of a cryostat for low temperature mechanical testing for the Mechanical and Materials Engineering group at
756 CERN. IOP Conference Series: Materials Science and Engineering 102.

757 Barabash, V., The ITER International Team, Peacock, A., Fabritsiev, S., Kalinin, G., Zinkle, S., Rowcliffe, A., Rensman,
758 J.W., Tavassoli, A., Marmy, P., et al., 2007. Materials challenges for ITER–Current status and future activities. Journal
759 of Nuclear Materials 367, 21–32.

760 Beese, A.M., Mohr, D., Santacreu, P.O., 2009. Isotropic phase transformation in anisotropic stainless steel 301LN sheets.
761 European Symposium on Martensitic Transformations .

762 Behjati, P., Najafizadeh, A., Kermanpur, A., 2011. Microstructural investigation on strengthening mechanisms of
763 AISI 304L austenitic stainless steel during cryogenic deformation. Materials Science and Technology 27, 1828–32.

764 Bertinelli, F., Fudanoki, F., Komori, T., Peiro, G., Rossi, L., 2006. Production of austenitic steel for the LHC supercon-
765 ducting dipole magnets. IEEE Transactions on Applied Superconductivity 16, 1773–6.

766 Botshekan, M., Degallaix, S., Desplanques, Y., 1997. Influence of martensitic transformation on the low-cycle fatigue
767 behaviour of 316LN stainless steel at 77 K. Materials Science and Engineering: A 234, 463–6.

768 Botshekan, M., Degallaix, S., Desplanques, Y., Polak, J., 1998. Tensile and LCF properties of AISI 316LN SS at 300 and
769 77 K. Fatigue & Fracture of Engineering Materials & Structures 21, 651–60.

770 Brüning, O., Burkhardt, H., Myers, S., 2012. The large hadron collider. Progress in Particle and Nuclear Physics 67,
771 705–34.

772 Chan, J., Chu, D., Tseng, C., Morris, J., 1994. Cryogenic fracture behavior of 316LN in magnetic fields up to 14.6 T, in:
773 Advances in Cryogenic Engineering Materials. Springer, pp. 1215–21.

774 Cooper, A.J., Brayshaw, W.J., Sherry, A.H., 2018. Effect of temperature on the fracture toughness of hot isostatically
775 pressed 304L stainless steel. Metallurgical and Materials Transactions A 49, 811–6.

776 Couturier, K., Sgobba, S., 2000. Phase stability of high manganese austenitic steels for cryogenic applications. Technical
777 Report. CERN, Switzerland.

778 Czarkowski, P., Krawczynska, A., Slesinski, R., Brynk, T., Budniak, J., Lewandowska, M., Kurzydlowski, K., 2011. Low
779 temperature mechanical properties of 316L type stainless steel after hydrostatic extrusion. Fusion Engineering and
780 Design 86, 2517–21.

781 De, A.K., Murdock, D.C., Mataya, M.C., Speer, J.G., Matlock, D.K., 2004. Quantitative measurement of deformation-
782 induced martensite in 304 stainless steel by X-ray diffraction. Scripta Materialia 50, 1445–9.

783 DeMania, D.A., 1995. The influence of martensitic transformation on the formability of 304L stainless steel sheet. Ph.D.
784 thesis. Massachusetts Institute of Technology, MA, United States.

785 Devred, A., Backbier, I., Bessette, D., Bevillard, G., Gardner, M., Jong, C., Lillaz, F., Mitchell, N., Romano, G., Vostner,
786 A., 2014. Challenges and status of ITER conductor production. Superconductor Science and Technology 27.

787 Drexler, E., Simon, N., Reed, R., 1994. Strength and toughness at 4 K of forged, heavy-section 316LN, in: Advances in
788 Cryogenic Engineering Materials. Springer, pp. 1199–206.

789 EN-10088-2, 2008. Stainless steels - Part 2: Technical delivery conditions for sheet/plate and strip of corrosion resisting
790 steels for general purposes.

791 Fava, J.O., Carabedo, F.D., Spinosa, C., Ruch, M.C., 2018. Assessment of the amount of deformation induced martensite:
792 a calibration curve for the Ferritoscope, in: 12th European Conference on Non-Destructive Testing (ECNDT).

793 FERITSCOPE-FMP30, 2008. Operator Manual. Helmut Fischer GmbH Institutfür Elektronik und Messtechnik, Sin-
794 delfingen Germany.

795 Fultz, B., Morris Jr, J., 1986. Effects of high magnetic fields on the flow stress of 18-8 stainless steels. Acta Metallurgica
796 34, 379–84.

797 Garion, C., Skoczeń, B., 2002. Modeling of plastic strain-induced martensitic transformation for cryogenic applications.
798 Journal of Applied Mechanics 69, 755–62.

799 Garion, C., Skoczeń, B., Sgobba, S., 2006. Constitutive modelling and identification of parameters of the plastic strain-
800 induced martensitic transformation in 316L stainless steel at cryogenic temperatures. International Journal of Plasticity
801 22, 1234–64.

802 Hecker, S.S., Stout, M.G., Staudhammer, K.P., Smith, J.L., 1982. Effects of strain state and strain rate on deformation-
803 induced transformation in 304 stainless steel: Part I. magnetic measurements and mechanical behavior. Metallurgical
804 Transactions A 13, 619–26.

805 Herrera, R., Landes, J., 1990. Direct JR curve analysis: a guide to the methodology, in: Fracture mechanics: twenty-first
806 symposium, ASTM International.

807 Hünicke, U.D., 2000. Neue Methoden zur Beurteilung der Umformeigenschaften von Feinblechen aus nichtrostenden
808 Edelstahlwerkstoffen, Teil I: Werkstoffkundliche Untersuchungen. Technical Report. University of Rostock, Germany.

809 ISO-6892-1, 2009. Metallic materials-Tensile testing-Part 1: Method of test at room temperature.

810 ISO-6892-3, 2015. Metallic materials-Tensile testing-Part 3: Method of test at low temperature.

811 ISO-6892-4, 2015. Metallic materials-Tensile testing-Part 4: Method of test in liquid helium.

812 Joyce, J.A., 2001. Analysis of a high rate round robin based on proposed annexes to ASTM E 1820. Journal of Testing
813 and Evaluation 29, 329–51.

814 Krauth, H., Nyilas, A., 1980. Fracture toughness of nitrogen strengthened austenitic steels at 4 K, in: Fracture and
815 Fatigue. Elsevier, pp. 119–28.

816 Landes, J., Zhou, Z., Lee, K., Herrera, R., 1991. Normalization method for developing J-R curves with the LMN function.
817 Journal of testing and evaluation 19, 305–11.

818 Lee, H., Shin, J., Shin, H., 1998. Fracture toughness of structural materials for LNG storage tank at cryogenic tempera-
819 tures. 한국가스학회: 학술대회논문집 , 340–9.

820 Lee, K., 1995. Elastic-plastic fracture toughness determination under some difficult conditions. Ph.D. thesis. University
821 of Tennessee-Knoxville, TN, United States.

822 Lopez, J.J., Miller, C., Tegtmeier, E.L., 2019. A test of ASTM Methods E1245-03 and E562-11 in calculating the volume
823 fraction of carbides in a U-10Mo foil. Technical Report. Los Alamos National Lab.(LANL), Los Alamos, NM, United
824 States.

825 Malik, N., 2021. Development of a universal cryogenic test facility. Master's thesis. Delft University of Technology, The
826 Netherlands.

827 Mangonon, P., Thomas, G., 1970. The martensite phases in 304 stainless steel. Metallurgical Transactions 1.

828 Mazandarany, F., Parker, D., Koenig, R., Read, D., 1980. A nitrogen-strengthened austenitic stainless steel for cryogenic
829 magnet structures, in: Advances in Cryogenic Engineering Materials. Springer, pp. 158–70.

830 McRae, D., Balachandran, S., Walsh, R., 2017. Fatigue and fracture of three austenitic stainless steels at cryogenic
831 temperatures, in: IOP Conference Series: Materials Science and Engineering.

832 Mei, Z., Morris Jr, J.W., 1990. Influence of deformation-induced martensite on fatigue crack propagation in 304-type
833 steels. Metallurgical Transactions A 21, 3137–52.

834 Mitchell, N., Bessette, D., Gallix, R., Jong, C., Knaster, J., Libeyre, P., Sborchia, C., Simon, F., 2008. The ITER magnet
835 system. IEEE Transactions on Applied Superconductivity 18, 435–40.

836 Morris Jr, J.W., Chan, J.W., Mei, Z., 1992. The influence of deformation-induced martensite on the cryogenic behavior
837 of 300-series stainless steels. Technical Report. Lawrence Berkeley Lab., CA, United States.

838 Murase, S., Kobatake, S., Tanaka, M., Tashiro, I., Horigami, O., Ogiwara, H., Shibata, K., Nagai, K., Ishikawa, K., 1993.
839 Effects of a high magnetic field on fracture toughness at 4.2 K for austenitic stainless steels. Fusion Engineering and
840 Design 20, 451–4.

841 Muster, W., Elster, J., 1990. Low temperature embrittlement after ageing stainless steels. Cryogenics 30, 799–802.

842 Naraghi, R., 2009. Martensitic transformation in austenitic stainless steels. Master's thesis. Royal Institute of Technology,
843 Stockholm, Sweden.

844 Nyilas, A., Mitterbacher, H., 2010. Fracture mechanical measurements with commercial stainless steels at 4 K and with
845 CP-titanium at 173 K, in: AIP Conference Proceedings, American Institute of Physics. pp. 33–40.

846 Nyilas, A., Obst, B., Harries, D., 1998. Mechanical investigations on aged stainless steel and Incoloy 908 materials at
847 4.2 K and 7 K, in: Advances in Cryogenic Engineering Materials. Springer, pp. 17–24.

848 Nyilas, A., Yanagi, H., 1989. 4 K fracture toughness investigations of 316LN stainless steel plate and forging materials.
849 Cryogenics 29, 191–5.

850 Obst, B., Nyilas, A., 1991. Experimental evidence on the dislocation mechanism of serrated yielding in FCC metals and
851 alloys at low temperatures. Materials Science and Engineering: A 137, 141–50.

852 Obst, B., Pattanayak, D., 1982. Discontinuous deformation modes of a nitrogen-stabilized austenitic steel, in: Advances
853 in Cryogenic Engineering Materials. Springer, pp. 57–65.

854 Ogata, T., Ishikawa, K., Nagai, K., 1985. Effects of strain rate on the tensile behavior of stainless steels, copper, and an
855 aluminium alloy at cryogenic temperatures. Tetsu-to-Hagane 71, 1390–7.

856 Ogata, T., Nagai, K., Ishikawa, K., Shibata, K., Murase, S., 1992. VAMAS second round robin test of structural materials
857 at liquid helium temperature, in: Materials. Springer, pp. 69–76.

858 Ogata, T., Umezawa, O., Ishikawa, K., 1990. Low temperature creep behaviour of stainless steels. Advances in Cryogenic
859 Engineering: Materials 36, 1233–9.

860 Olson, G., Cohen, M., 1975. Kinetics of strain-induced martensitic nucleation. Metallurgical Transactions A 6.

861 Onyuna, M.O., 2003. Deformation behaviour and martensitic transformations in metastable austenitic steels and low
862 alloyed multiphase steels. Ph.D. thesis. Freiberg University of Mining and Technology, Germany.

863 Ortwein, R., 2015. Constitutive model of graded micro-structure obtained via strain induced phase transformation. Ph.D.
864 thesis. Cracow University of Technology, Poland.

865 Park, J., Lee, K., Sung, H., Kim, Y.J., Kim, S.K., Kim, S., 2019. J-integral fracture toughness of high-Mn steels at room
866 and cryogenic temperatures. Metallurgical and Materials Transactions A 50, 2678–89.

867 Park, S.H., Kim, J.Y., Park, W.W., Choi, H., Ma, Y.J., Kwon, S.P., Kim, K., Kang, S.C., Lee, D.H., 2011. The effect
868 of plastic deformation on low temperature mechanical and magnetic properties of austenite 316LN tube for ITER TF
869 conductor. IEEE Transactions on Applied Superconductivity 22.

870 Pattanayak, D., 1984. The influence of prestrain and transformation mode on the mechanical properties of nitrogen
871 stabilized austenitic steel, in: Advances in Cryogenic Engineering Materials. Springer, pp. 227–36.

872 Peterson, S.F., 1996. Formability of austenitic stainless steels. Master's thesis. Colorado School of Mines, CO, United
873 States.

874 Purtscher, P., Read, D., 1987. Effect of prior deformation on the 76-K fracture toughness of AISI 304L and AWS 308L
875 stainless steels. ASME Journal of Engineering Materials and Technology 109, 151–6.

876 Reed, R.P., 1989. Nitrogen in austenitic stainless steels. The Journal Of The Minerals, Metals & Materials Society 41,
877 16–21.

878 Rintamaa, R., 1981. The effects of austenite stability on the formability of austenitic stainless steels. Ph.D. thesis.
879 Helsinki University of Technology, Laboratory of Processing and Heat Treatment of Materials, Finland.

880 Rosenthal, Y.A., Tobler, R.L., Purtscher, P.T., 1990. $J_{Ic}$ data analysis methods with a "negative crack growth" correction
881 procedure. Journal of Testing and Evaluation 18, 301–4.

Sa, J.W., Kim, H.K., Choi, C.H., Kim, H.T., Hong, K.H., Park, H.K., Bak, J.S., Lee, K.W., Ha, E.T., 2005. Mechanical characteristics of austenitic stainless steel 316LN weldments at cryogenic temparature, in: 21st IEEE/NPS Symposium on Fusion Engineering SOFE 05, IEEE. pp. 1–4.

Self, J., Olson, D.L., Edwards, G.R., 1987. The stability of austenitic weld metal. NBS Publication on Cryogenic Properties of Metals , 181–9.

Seok, C.S., 2000. Correction methods of an apparent negative crack growth phenomenon. International Journal of Fracture 102, 259–69.

Sgobba, S., 2006. Materials for high vacuum technology, an overview. Technical Report. CERN, Switzerland.

Shimada, M., Ogawa, R., Horiuchi, T., 1987. Effects of aging on cryogenic mechanical properties of low carbon austenitic stainless steels. Journal of Cryogenics and Superconductivity Society of Japan 22, 265–71.

Skoczeń, B., 2001. Stability, fatigue and optimization of thin-walled structures under cryogenic conditions: Application in the structural design of colliders and cryogenic transfer lines. CERN-2001-001, CERN.

Spencer, K., Embury, J.D., Conlon, K.T., Véron, M., Bréchet, Y., 2004. Strengthening via the formation of strain-induced martensite in stainless steels. Materials Science and Engineering: A 387, 873–81.

Tabin, J., Skoczeń, B., Bielski, J., 2016. Strain localization during discontinuous plastic flow at extremely low temperatures. International Journal of Solids and Structures 97, 593–612.

Talonen, J., 2007. Effect of strain-induced $\alpha$'-martensite transformation on mechanical properties of metastable austenitic stainless steels. Ph.D. thesis. Helsinki University of Technology, Finland.

Talonen, J., Aspegren, P., Hänninen, H., 2004. Comparison of different methods for measuring strain induced $\alpha$-martensite content in austenitic steels. Materials Science and Technology 20, 1506–12.

Tarafder, M., Tarafder, S., 2006. Modelling of Crack-tip Blunting using Finite Element Method (FEM) (GAP-0088). Technical Report. National Metallurgical Laboratory, Jamshedpur, India.

Vander Voort, G.F., Lampman, S.R., Sanders, B.R., Anton, G.J., Polakowski, C., Kinson, J., Muldoon, K., Henry, S.D., Scott Jr, W.W., 2004. ASM Handbook. Volume 9: Metallography and Microstructures. ASM International, Materials Park, OH, United States.

Vogt, J., Foct, J., Regnard, C., Robert, G., Dhers, J., 1991. Low-temperature fatigue of 316L and 316LN austenitic stainless steels. Metallurgical Transactions A 22, 2385–92.

909 Voss, B., 1983. On the problem of “negative crack growth” and “load relaxation” in single specimen partial unloading
910 compliance tests, in: Ductile fracture test methods.

911 Wang, S., Yang, K., Shan, Y., Li, L., 2008. Plastic deformation and fracture behaviors of nitrogen-alloyed austenitic
912 stainless steels. Materials Science and Engineering: A 490, 95–104.

913 Wang, W., Yan, W., Yang, K., Shan, Y., Jiang, Z., 2010. Temperature dependence of tensile behaviors of nitrogen-alloyed
914 austenitic stainless steels. Journal of Materials Engineering and Performance 19, 1214–9.

915 Weiss, K., Nyilas, A., 2006. Specific aspects on crack advance during J-test method for structural materials at cryogenic
916 temperatures. Fatigue & Fracture of Engineering Materials & Structures 29, 83–92.

917 Yanushkevich, Z., Dobatkin, S., Belyakov, A., Kaibyshev, R., 2017. Hall-Petch relationship for austenitic stainless steels
918 processed by large strain warm rolling. Acta Materialia 136, 39–48.

919 Zheng, C., Liu, C., Ren, M., Jiang, H., Li, L., 2018. Microstructure and mechanical behavior of an AISI 304 austenitic
920 stainless steel prepared by cold-or cryogenic-rolling and annealing. Materials Science and Engineering: A 724, 260–8.